

UNCLASSIFIED

AD NUMBER

ADA181005

LIMITATION CHANGES

TO:

Approved for public release; distribution is unlimited.

FROM:

Distribution authorized to U.S. Gov't. agencies and their contractors;
Administrative/Operational Use; MAR 1987. Other requests shall be referred to Office of Naval Research, 875 Randolph Street, Arlington, VA 22203-1995.

AUTHORITY

ONR ltr, 15 May 1987

THIS PAGE IS UNCLASSIFIED

Brown University,
Division of Engineering
Providence, R.I. 02912

ELASTIC-PLASTIC ANALYSIS OF
CRACKS ON BIMATERIAL
INTERFACES,

PART I: SMALL SCALE
YIELDING,

by

C. F. Shih and R. J. Asaro

ONR Contract
"Mechanics of Interface Cracks"
March 1987

ABSTRACT

Full field numerical solutions for a crack which lies along the interface of an elastic-plastic medium and a rigid substrate are presented. The solutions are obtained using a small strain version of the J_2 deformation theory with power law strain hardening. In the present article results for loading causing only *small scale yielding* at the crack tip are described; in a subsequent article results for contained yielding and fully plastic behavior will be presented. The oscillatory stresses on the bond line and overlapping of the crack faces, characteristic of small strain linear elasticity, are shown to be essentially precluded by material nonlinearity. In addition we find that, although the near tip fields do not appear to have a separable form as for the well known HRR fields in homogeneous media, they do bear interesting similarities to certain mixed mode HRR fields. Numerical procedures appropriate for solving a general class of interface crack problems are described. A description of a numerical method for extracting the mixed mode stress intensities for cracks at interfaces, and in homogeneous isotropic or anisotropic media, is included.

1. INTRODUCTION

Fracture, whether it occurs by fibrous or cleavage modes, invariably begins at interfaces. In structural alloys, precipitation or segregation of impurities at grain boundaries can lead to transitions from ductile to cleavage fracture and to concomitant losses in ductility and toughness. In so-called *advanced materials* such as structural ceramics, composites, and polycrystalline intermetallic alloys, interfacial and intergranular fractures are common and may, in large part, determine the material's overall mechanical response. At present, however, what exists is only a relatively small group of solutions for the crack tip fields at the interfaces of isotropic linear elastic media (e.g. Williams, 1959; Erdogan, 1963, 1965; Sih and Rice, 1964; Rice and Sih, 1965; England, 1965). A formal solution for the field of an isolated crack lying along the interface of linear anisotropic media has been given by Willis (1971) which, while perhaps not lending itself to a ready evaluation of the nature of the field, does allow for a computation of the energy release rate for crack extension along the interface. To our knowledge there are no solutions for the fields of interface cracks in elastic-plastic materials and this makes it difficult to analyze the legion of interface fracture phenomena alluded to above. One purpose of this study is to provide such solutions within a framework consistent with what exists for nonlinear fracture mechanics in homogeneous materials (Hutchinson, 1983). Another is to develop numerical procedures capable of accurately resolving the complex fields which develop at interfaces. Our presentation is to be given in two parts: in the present paper the structure of the asymptotic field under small scale yielding conditions is described; the fields that develop under contained yielding and fully plastic conditions will be presented in a subsequent publication. Implications of the characteristic stress and deformation fields that form at and near interfaces for fracture mechanics will be detailed in the latter.

Specifically, the plane strain boundary value problem for a center cracked plate loaded with uniform remote stresses is solved and discussed here. This is illustrated along with a version of the finite element mesh used for numerical solution in Fig. 3. The crack lies

on the interface between a rigid substrate and a nonlinear elastic-plastic material characterized by a J_2 deformation theory. This problem serves as a prototype for a wide class of physically interesting phenomena involving microcracking and macroscopic fracture, while at the same time allowing for an unambiguous and definitive study of the structure of the fields of interface cracks within the context of a complete boundary value problem. Crack tip fields have been evaluated numerically for linear elastic materials and nonlinear elastic-plastic materials (characterized by a small strain J_2 deformation theory) under small scale yielding, contained yielding, and fully-plastic conditions. In the present paper attention is focused on elastic behavior and elastic-plastic behavior under small scale yielding. For this analysis a domain formulation of an interaction energy release rate is employed to extract the complex stress intensity factors from the numerical fields. Some discussion of results for contained yielding is provided, but as noted above, a full treatment of these cases along with the fields for cracks under loading conditions that cause fully yielded behavior will be given in a subsequent article.

In the context of interface cracks, small scale yielding is meant to pertain to loading conditions for which the plastic zone emanating from the crack tip is surrounded by elastic fields which are well approximated by the elastic singularity fields for the interface crack. We do not suggest that the plastic zones develop in a self-similar manner as they do for cracks in homogeneous media. Indeed the change in plastic zone size and shape with increasing remote stress is detailed in Sections 4.3, and this should be kept in mind in interpreting the results presented in Sections 4.3 and 5.

As mentioned, the calculations are performed for a material described by a small strain, isotropic J_2 deformation theory. This was done in order to facilitate the connection between the interface crack solutions, the existing framework of nonlinear fracture mechanics, and specific solutions for crack tip fields in homogeneous media. Both qualitative and quantitative similarities between the fields are highlighted in the

results we present. It is found, for example, that the near-tip stress and strain fields are inherently mixed mode regardless of the far-field loading. Although the fields for the interface crack are not of the usual separable form, there are nonetheless strong similarities between them and the mixed mode fields for cracks in homogeneous media. (Thus far, our attempts to find fields near the tip of an interface crack which are of a separable form have not been successful.) These features have important implications for the mathematical characterization of the fields as well as for failure processes that may be induced at or near the interface.

We note, however, that the stress histories that develop near the tip of the interface crack cannot be described as proportional stressing. At low remote stress levels, for example, the fields that develop near the tip are of a strongly mixed mode nature - reflecting the mixed mode character of the linear elastic field. At higher remote stresses our results show that the crack tip fields are more nearly like those corresponding to pure mode I fields of cracks in homogeneous media. The transition from strongly mixed mode fields to nearly mode I fields certainly involves non-proportional stressing. Thus interface crack tip behavior is more complex than is found for cracks in homogeneous media for which proportional remote loading induces proportional stressing near the crack tip. The link between the fields calculated here for a J_2 deformation theory material and those appropriate to path-dependent incremental elastic-plastic theories is the subject of the current investigation.

The plan of the paper is as follows. In the next section we present a summary of available results for crack tip stress and displacement fields in linear isotropic media. This introduces the notion of a stress concentration vector, or stress intensity factors, for interface cracks and provides the requisite background to analyze the elastic-plastic results. A complete description of the boundary value problem to be solved is also given. Numerical methods are then described, followed by the presentation of the full field solutions. A short discussion on the nature of the computed fields concludes this paper.

2. PERSPECTIVES ON CRACKS AT BIMATERIAL INTERFACES

2.1 Overview of Results for Linear Elastic Media

A number of solutions for the stress and displacement fields for cracks lying along bimaterial interfaces have been obtained for isotropic materials by, for example, Williams (1959), England (1965), Erdogan (1963,1965), Sih and Rice (1964) and Rice and Sih (1965). For anisotropic materials Willis (1971) has provided a formal solution which allows the energy release rate to be evaluated. Our concern in this section is to illustrate the nature of the tractions and the displacement discontinuities on the crack line at the crack tip, identify stress intensity factors and relate them to energy release rates. The discussion is confined to isotropic elastic media where the results are easily represented in a concise structure.

We refer to Fig. 1 which shows a crack lying along an interface separating media 1 and 2. The shear moduli and Poisson's ratios are μ_1, μ_2 and ν_1, ν_2 . ξ is the distance measured along the bond line from the crack tip such that $\xi = r$, the polar coordinate, when $\theta = 0$ and $\theta = \pi$. In what follows it is to be understood that ξ is directed along the bond line in the expressions for tractions, whereas it is directed back along the crack faces in the expressions given below for the displacement jumps across the crack face. Existing solutions show that the tractions on the bond line can be expressed in the form

$$\sigma_{22} = \frac{K_1 \cos(\epsilon \ln(\xi/2a))}{\sqrt{2\pi\xi}} - \frac{K_2 \sin(\epsilon \ln(\xi/2a))}{\sqrt{2\pi\xi}} \quad (2.1a)$$

and

$$\sigma_{12} = \frac{K_1 \sin(\epsilon \ln(\xi/2a))}{\sqrt{2\pi\xi}} + \frac{K_2 \cos(\epsilon \ln(\xi/2a))}{\sqrt{2\pi\xi}} \quad (2.1b)$$

where ϵ is the bimaterial constant introduced by Williams (1959), Erdogan (1963), Sih and Rice (1964), and England (1965), defined as

$$\epsilon \equiv \frac{1}{2\pi} \ln \left\{ \frac{\frac{3-4\nu_1}{\mu_1} + \frac{1}{\mu_2}}{\frac{1}{\mu_1} + \frac{3-4\nu_2}{\mu_2}} \right\}. \quad (2.2)$$

K_1 and K_2 define two stress intensity factors which, we note, have units of stress-(length)^{1/2} in analogy with the definition of stress intensity factors in homogeneous media. It is convenient to introduce a *complex stress intensity factor* defined by $K = K_1 + iK_2$. This definition is related in a simple way to others available in the literature and, for example, is related to the complex stress intensity factor of Sih and Rice (1964), $k = k_1 + ik_2$, by $K = \sqrt{\pi} \cosh(\pi\epsilon)(2a)^{i\epsilon} k$.

Combining (2.1) as in the original solutions cited above (see also Willis' (1971) eq. (4.4)), the tractions on the bonding surface can also be expressed as the complex vector

$$t = \sigma_{22} + i \sigma_{12} = \frac{K}{\sqrt{2\pi\xi}} e^{i\epsilon \ln(\xi/2a)} = \frac{K}{\sqrt{2\pi\xi}} (\xi/2a)^{i\epsilon} \quad (2.3)$$

Explicit examples of K for three crack geometries and loading configurations, taken from the above references, are given in Fig. 2. We note that, in general, the two stress modes defined by K_1 and K_2 each involve mixed tension and shear on the bonding surface and, in isotropic media, represent orthogonal modes. That is, if

$$t_1 \equiv \frac{K_1}{\sqrt{2\pi\xi}} e^{i\epsilon \ln(\xi/2a)}, \quad (2.4a)$$

then

$$t_2 = \frac{K_2}{\sqrt{2\pi\xi}} e^{i\{\epsilon \ln(\xi/2a) + \pi/2\}} \quad (2.4b)$$

which is oriented at a right angle to t_1 when plotted on a graph with σ_{22} on the real axis and σ_{12} on the imaginary axis. When the two media are identical, $\epsilon = 0$ and K_1 and K_2 reduce to the usual mode I and II stress intensity factors, K_I and K_{II} .

Displacement jumps across the crack face have also been given (explicitly by England, 1965) and, at the crack tip, take the form,

$$\Delta U = \Delta u_2 + i \Delta u_1 = \frac{2 \left\{ \frac{1-\nu_1}{\mu_1} + \frac{1-\nu_2}{\mu_2} \right\}}{(1+2i\epsilon) \cosh \pi\epsilon} \mathbf{K} \sqrt{\xi/2\pi} e^{i\epsilon \ln(\xi/2a)} \quad (2.5)$$

This can also be written as

$$\Delta U = \frac{2 \left\{ \frac{1-\nu_1}{\mu_1} + \frac{1-\nu_2}{\mu_2} \right\}}{(1+4\epsilon^2)^{1/2} \cosh \pi\epsilon} \mathbf{K} \sqrt{\xi/2\pi} (\xi/2a)^{i\epsilon} e^{-i\beta} \quad (2.6)$$

where $\beta = \tan^{-1} 2\epsilon$. Thus the contributions to ΔU associated with the stress modes K_1 and K_2 (call them ΔU_1 and ΔU_2) are also orthogonal but are not precisely aligned with \mathbf{t}_1 and \mathbf{t}_2 . In fact, if \mathbf{t}_1 and \mathbf{t}_2 are placed on a graph whose axes are σ_{22} and σ_{12} then the orthogonal pair $\Delta U_1, \Delta U_2$, when graphed with respect to axes Δu_2 and Δu_1 , would appear to be rigidly rotated with respect to the orthogonal pair $\mathbf{t}_1, \mathbf{t}_2$ by the angle β .

As noted by Williams (1959), and in subsequent works, a characteristic of the linear elastic fields of interface cracks is that they violate compatibility at distances very close to the tip; the stresses and displacement fields on the crack line oscillate with unbounded amplitude and vanishing wavelength. Looking ahead to the problem of the center cracked panel under far field tension that we investigate numerically, we note that Rice and Sih's (1965) results yield the stress intensity vector $\mathbf{K} = \sigma_{22}^{\infty} \sqrt{\pi a} (1+2i\epsilon)$. This means, for example, that the normal tractions on the bond line become compressive as soon as

$$\text{Re} \left\{ (1+2i\epsilon) e^{i\epsilon \ln(\xi/2a)} \right\} < 0, \quad (2.7)$$

or using the definition for β introduced earlier, when

$$\text{Re} \left\{ e^{i[\epsilon \ln(\xi/2a) + \beta]} \right\} < 0. \quad (2.8)$$

Since $(\xi/2a) < 1$, this first occurs as soon as

$$\epsilon \ln(\xi/2a) + \beta < -\pi/2 \quad (2.9)$$

Thus $\sigma_{\theta\theta}$ first becomes compressive at

$$(\xi/2a) = e^{-[\pi/2+\beta]/\epsilon} \quad (2.10)$$

For the case of a crack on a rigid substrate, where in the deformable half space $\nu = 0.3$, $\epsilon \cong 0.0935$, and this leads to a value of $\xi/2a \cong 7 \times 10^{-9}$. Our numerical results reproduced this (albeit *non-physical*) feature of the linear elastic field. In fact, looking ahead to Fig. 8, where the numerical solution for the interface crack in a linear elastic medium is presented, it may be noted that along a ray at an angle of 7.5° with the bond line (i.e. essentially on the bond line) $\sigma_{\theta\theta}$ becomes compressive at $r/a \cong 1 \times 10^{-9}$ which is completely consistent with this stress component first becoming compressive at $\xi/a \cong 14 \times 10^{-9}$ at $\theta = 0^\circ$. However, we note that when the loading is a combined remote tension and shear, $\mathbf{K} = [(\sigma_{22}^\infty - 2\sigma_{12}^\infty\epsilon) + i(\sigma_{12}^\infty + 2\epsilon\sigma_{22}^\infty)]\sqrt{\pi a}$ and a similar analysis shows that $\sigma_{\theta\theta}$ first becomes compressive on the bond line when

$$(\xi/2a) = e^{-[\pi/2 + \lambda]/\epsilon} \quad (2.11)$$

where

$$\lambda = \tan^{-1}\{(\sigma_{12}^\infty + 2\epsilon\sigma_{22}^\infty)/(\sigma_{22}^\infty - 2\epsilon\sigma_{12}^\infty)\}. \quad (2.12)$$

Now suppose $\sigma_{22}^\infty > 0$ but $\sigma_{12}^\infty = -2\sigma_{22}^\infty$; then $\lambda \cong -58.7^\circ$ and $\xi/2a \cong 1 \times 10^{-3}$! If $\sigma_{12}^\infty = -\sigma_{22}^\infty$, $\lambda \cong -38.2^\circ$ and $\xi/2a \cong 3 \times 10^{-5}$. Thus the regions where the stresses (based on small strain linear elasticity assumptions) oscillate are not always confined to vanishingly small regions near the crack tip and their extents are quite sensitive to the nature of the remote loading and the value of ϵ . In Section 5 full field results are presented for the interface crack in nonlinear materials subjected to remote *mixed* loadings. They demonstrate that such oscillations are not present when the remote stresses are small fractions of the material's yield stress. This is also shown, in detail, in Section 4 for the case of pure remote

tensile loading. It may be noted that when $\nu = 1/2$, $\epsilon = 0$ and the near-tip displacements vanish identically on the bond line for the plane strain problem. For this case the fields are non-oscillatory and are identical to the fields for the corresponding homogeneous media. This fact has been noticed by Knowles and Sternberg (1983).

When written out in full the asymptotic crack tip stress field is given by

$$\sigma_{ij} = \sum_{\alpha=1}^2 \frac{K_{\alpha}}{(2\pi r)^{1/2}} g_{ij}^{(\alpha)} [\theta, \epsilon/\ln(r/2a); \epsilon] \quad (2.13)$$

and, for completeness, the functions $g_{ij}^{(\alpha)}$ are given in Appendix I in a form consistent with our definition of the complex stress intensity vector \mathbf{K} . It should be noted that the fields (2.13) are not of a separable form. In contrast, the singular fields of cracks in homogeneous media are separable. It should also be noted that with our definition of the complex stress intensity factor, crack geometry appears in the angular functions as well as in the stress intensity factors.

The energy release rate is readily computed from the given expressions for the traction and displacement fields as the *virtual work integral*

$$G = \lim_{\Delta a \rightarrow 0} \frac{1}{2\Delta a} \int_0^{\Delta a} \mathbf{t}(\xi; 0) \cdot \Delta \bar{\mathbf{U}}(\xi; 0 + \Delta a) d\xi \quad (2.14)$$

where $\mathbf{t}(\xi; 0)$ is the complex traction vector at the crack tip, given by (2.3), when the crack is at $x = 0$, and $\Delta \bar{\mathbf{U}}(\xi; 0 + \Delta a)$ is the complex conjugate to the displacement jump vector when the crack has advanced to the position $0 + \Delta a$. The integral is easily reduced to the form

$$\frac{|\mathbf{K}|^2 \left\{ \frac{1-\nu_1}{\mu_1} + \frac{1-\nu_2}{\mu_2} \right\}}{2\pi \cosh \pi\epsilon} \times \frac{1}{(1-2i\epsilon)} \int_0^1 \left[\frac{1-t}{t} \right]^{1/2-i\epsilon} dt \quad (2.15)$$

where the last integral is recognizable as the complex Beta function $B(1/2+i\epsilon, 3/2-i\epsilon)$. Upon evaluation of B,

$$G = \frac{(K_1^2 + K_2^2) \left\{ \frac{1-\nu_1}{\mu_1} + \frac{1-\nu_2}{\mu_2} \right\}}{4\cosh^2 \pi\epsilon} \quad (2.16)$$

Orthogonality of the stress modes guarantees that they decouple such that there are no terms of the form $K_1 K_2$. Note also that the integral in (2.14) has no imaginary part, a fact noticed in the general anisotropic case by Willis (1971).

List of stress intensity factors

We complete this section with the short list of stress intensity factors tabulated in Fig. 2. Included in this list is the center cracked panel we have studied numerically. It may be noted in these examples that with K defined by (2.3), the ratio of K_1 to K_2 does not depend on the characteristic dimension $2a$.

2.2 The Interface Crack Small Scale Yielding Problem

The specific problem we are concerned with here, illustrated in Fig. 3, is that of a large plate loaded remotely by uniform stresses. Crack length, $2a$, is the characteristic dimension with respect to which the stress intensity factors listed in Fig. 2, and the asymptotic angular stress functions given in Appendix I, are evaluated. Uniform normal stresses are imposed on the external boundaries with the primary variable being σ_{22}^∞ . No remote shear is imposed although, as is evident from the elastic solutions, large shear stresses develop on and near the crack line due to the differences in material properties. This is also true for the elastic-plastic cases treated numerically.

As noted by Rice and Sih (1965), continuity of the extensional strain ϵ_{11} across the bond line requires that the normal stress parallel to the bond line be discontinuous. They derived the required jump in σ_{11}^∞ , viz.

$$\sigma_{11}^{\infty}(2) = \omega \sigma_{11}^{\infty}(1) + \frac{(3+\omega)e^{2\pi\epsilon} - (3\omega+1)}{1+e^{2\pi\epsilon}} \sigma_{22}^{\infty} \quad (2.17)$$

where

$$\omega = \frac{\mu_2(1-\nu_1)}{\mu_1(1-\nu_2)} \quad (2.18)$$

For the present case of the crack on the rigid substrate, $\omega \rightarrow \infty$ and the above relation takes the form

$$\sigma_{11}^{\infty}(1) = \frac{3 - e^{2\pi\epsilon}}{1 + e^{2\pi\epsilon}} \sigma_{22}^{\infty} = \frac{\nu_1}{(1-\nu_1)} \sigma_{22}^{\infty} \quad (2.19)$$

In the numerical solutions described next the normal stress given by (2.19), for $\nu = 0.3$, was imposed on the side faces of the deformable medium shown in Fig. 3.

The small scale yielding study is carried out within the context of small strain theory. The deformable medium is taken to be described by J_2 deformation theory for a Ramberg-Osgood stress-strain behavior. In uniaxial tension the material deforms according to

$$\epsilon/\epsilon_0 = \sigma/\sigma_0 + \alpha(\sigma/\sigma_0)^n \quad (2.20)$$

where σ_0 and ϵ_0 are the reference stress and strain, α is a material constant (taken to be 0.1 in this study) and n is the strain hardening exponent. Under multi-axial stress states σ_{ij} , the strain is

$$\epsilon_{ij} = \frac{1+\nu}{E} s_{ij} + \frac{1-2\nu}{3E} \sigma_{kk} \delta_{ij} + \frac{3}{2} \alpha \left[\frac{\sigma_e}{\sigma_0} \right]^{n-1} \frac{s_{ij}}{E} \quad (2.21)$$

Here, s_{ij} is the stress deviator, $\sigma_e = (3s_{ij}s_{ij}/2)^{1/2}$ is the effective stress, and ν and E are the elastic constants. In writing (2.21) we have used the connection $\sigma_0 = \epsilon_0 E$. Numerical solutions under plane strain assumptions have been obtained for a range of hardening exponents. However, only results for $n=3$ (a high hardening material) and $n=10$ (a moderate to low hardening material) will be presented. In all the calculations we have used ν equal to 0.3.

3. NUMERICAL PROCEDURE

3.1 Selective Integration

The standard displacement-based serendipity and Lagrangian isoparametric quadrilateral elements perform poorly as the deformation progresses into the fully plastic (incompressible) range (Nagtegaal et al., 1974). These difficulties can be alleviated by selective/reduced integration and one implementation of this is the so-called *B-bar method* (Hughes, 1980). The strain-displacement matrix, referred to as the B matrix, is assembled in the following manner. The deviatoric components of the B matrix are evaluated at the regular quadrature points. Volumetric components are evaluated at the reduced quadrature points; the volumetric B matrix associated with the regular quadrature points is obtained by interpolation/extrapolation using a lower order shape function. The volumetric and deviatoric components are then combined to give the desired matrix associated with the regular quadrature points. The latter matrix, denoted by \bar{B} (to distinguish it from the usual B matrix, Zienkiewicz, 1977), is used in the formation of element stiffness matrix and for evaluating strains.

The full Lagrangian shape functions are necessary for approaching the incompressible limit (Malkus and Hughes, 1978). In this regard it appears that an optimal element for treating nearly incompressible deformation is the 9-node Lagrangian quadrilateral element. For this element the deviatoric part of B is evaluated at 3x3 Gaussian quadrature points while the volumetric part is evaluated at 2x2 quadrature points. The volumetric B at each of the 3x3 quadrature points is obtained by bilinear interpolation/extrapolation and combined with the deviatoric part to give \bar{B} , i.e.

$$\bar{B} = B^{\text{dev}} + \bar{B}^{\text{vol}} \quad (3.1)$$

The (tangent) stiffness matrix for an element is given by the sum of the inner products at each Gauss point,

$$k^e = \sum_{p=1}^9 (\bar{B}^T D \bar{B}) w_p. \quad (3.2)$$

where D is the matrix of material moduli evaluated at the 3×3 quadrature points and w_p is the appropriate weight. It is known that the selective integration method gives rise to a spurious pressure mode in the 4-node quadrilateral element. For this element, \bar{B}^{vol} is evaluated with one-point quadrature. Belytschko and Tsay (1983) have proposed a stabilization procedure to suppress such spurious modes. Spurious pressure modes are avoided by using the 9-node Lagrangian element.

We obtained results that are nearly identical in our numerical experimentations with the B-bar method and selective integration (2×2 quadrature on volumetric stiffness matrix and 3×3 quadrature on deviatoric stiffness matrix) on several boundary value problems based on the volume preserving plasticity relations (2.20). In this connection, it may be noted that accurate solutions to fully plastic crack problems in homogeneous media have been obtained using the 9-node Lagrangian element in conjunction with selective integration and parameter tracking (e.g. Shih and Needleman, 1984). For the present boundary value problem based on (2.21), the incompressibility constraint is more directly and efficiently accommodated by the B-bar method. In passing, we point out that the results plotted in the figures of this paper are the actual values computed at the quadrature points - smoothing has not been applied to any data.

3.2 Parameter Tracking

The solution to the nonlinear boundary value problem is obtained by the Newton-Raphson method. The iterative method is second order convergent if a close initial estimate of the solution is available. For highly nonlinear problems of the type being investigated here, the initial estimate is generated by parameter tracking. We begin by obtaining the solution to the linear elastic problem at the desired remote stress. The

linear elastic solution is then employed as the initial estimate in the iterations for the mildly nonlinear problem with $n=2$. The convergent solution for the mildly nonlinear problem is then employed as the initial estimate for a more nonlinear problem, say $n=3$. In this manner solutions for material characteristics ranging from high hardening to nearly non-hardening are obtained. Similar tracking is performed on the remote stress levels; that is once a convergent solution is obtained for a given remote loading and nonlinear material description, it may be used as the initial guess for a new solution at a higher remote load.

3.3 Domain Representation of J

We consider the line integral (Rice, 1968) defined by

$$J = \int_{\Gamma} \left[W \delta_{ij} - \sigma_{ij} \frac{\partial u_i}{\partial x_j} \right] n_j d\Gamma . \quad (3.3)$$

Here, Γ is a contour beginning at the bottom crack face and ending on the top face and n_j is the outward normal to Γ as shown in Fig. 4. For a nonlinear elastic solid or deformation theory solid, the integrand is divergence free. With regard to the crack between a deformable medium and a rigid substrate, the contour Γ begins on the bonding plane and ends on the upper crack face. Since there are no contributions to the integral along the traction free crack face and the interface $x_2 = 0^+$ (u_i vanishes on the bond line), the value of J does not depend on the contour Γ , i.e. the integral is path-independent. For the general bimaterial problem, the contour Γ begins on the lower crack face and ends on the upper crack face. Path-independence is easily demonstrated for this general case once it is recognized that the contribution from the upper interface, $x_2 = 0^+$, negates the contribution from the lower interface, $x_2 = 0^-$. For monotonic loading conditions and proportional stress history at each material point, the above integral is also path-independent for elastic-plastic solids.

For numerical purposes it is more advantageous to recast the line-integral (3.3) as an area/domain integral. Such a representation is naturally compatible with the finite element method and very accurate values for J have been obtained using the domain representation. A domain integral formulation for the crack tip force (including the J -integral) for general material response and arbitrary crack tip motion has been detailed by Moran and Shih (1986) and has been applied to several crack problems in homogeneous media (e.g. Li et al., 1985, Shih et al., 1986). To obtain the desired domain representation for J , weighting functions q_i are introduced. For two dimensional problems with the crack line oriented in the x_1 -direction, q_1 is the only non-zero function and it has the value of unity on the contour Γ and zero on the outer contour C_0 shown in Fig. 4. Within the area enclosed by Γ , C_0 and the crack faces C_+ and C_- , q_1 is an arbitrary smooth function of x_1 and x_2 with values in the range from zero to one. The function $q_1(x_1, x_2)$ may be interpreted as the virtual translation of the material point at (x_1, x_2) due to a unit virtual extension of the crack in the x_1 -direction. Development along these latter lines has been given by Parks, 1977, Hellen, 1975 and deLorenzi, 1982.

For a function q_1 that satisfies the above conditions, the integral in (3.3) can be restated as a line integral over the closed contour C which consists of Γ , C_0 and the crack faces defined by

$$J = \int_C \left[\sigma_{ij} \frac{\partial u_i}{\partial x_1} - W \delta_{1j} \right] m_j q_1 dC. \quad (3.4)$$

Here m_j are the components of the unit vector normal to C that points away from the enclosed area. On the contour Γ , m_j is equal to the negative of n_j which has been defined earlier. The crack faces are assumed to be traction free. Applying the divergence theorem to (3.4) and using the equation of equilibrium, the equivalent domain representation of (3.3) is

$$J = \int_A \left[\sigma_{ij} \frac{\partial u_i}{\partial x_j} - W \delta_{ij} \right] \frac{\partial q_1}{\partial x_j} dA \quad (3.5)$$

where A is the area enclosed by the closed contour C. In deriving the expression (3.5), W is taken to be a potential function of stress, i.e., $\sigma_{ij} = \partial W / \partial \epsilon_{ij}$.

3.4 Finite Element Representation of Domain J

The finite element form of the domain representation (3.5) is briefly discussed. In isoparametric (η_1, η_2) ($-1 \leq \eta_i \leq 1, i=1,2$) space, the shape functions are constructed from the basic functions

$$f_1 = -\frac{1}{2}\eta(1-\eta), \quad f_2 = (1-\eta)(1+\eta), \quad f_3 = \frac{1}{2}\eta(1+\eta) \quad (3.6)$$

via

$$N_{3J+I-3} = f_I(\eta_1) f_J(\eta_2), \quad I, J = 1, 2, 3. \quad (3.7)$$

The coordinates (x_1, x_2) in the physical space and the displacements (u_1, u_2) are given by

$$x_i = \sum_{K=1}^9 N_K X_{iK}, \quad u_i = \sum_{K=1}^9 N_K U_{iK} \quad i = 1, 2 \quad (3.8)$$

where X_{iK} are the nodal coordinates and U_{iK} are the nodal displacements.

The discrete form of J based on 3x3 Gaussian quadrature appropriate to the 9-node biquadratic Lagrange element is

$$J = \sum_{\substack{\text{all elements} \\ \text{in A}}} \sum_{p=1}^9 \left[\sigma_{ij} \frac{\partial u_j}{\partial x_i} - W \delta_{ij} \right] \frac{\partial q_1}{\partial x_i} \det \left[\frac{\partial x_k}{\partial \eta_k} \right] w_p \quad (3.9)$$

The field quantities, including q_1 and its spatial derivatives, are evaluated at the nine quadrature points and weighted by w_p and the determinant of Jacobian matrix,

$\det (\partial x_k / \partial \eta_k)$. To be consistent with the isoparametric formulation the values of q_1 and $\partial q_1 / \partial x_i$ at the quadrature points are evaluated from

$$q_1 = \sum_{I=1}^9 N_I Q_{1I}, \quad \frac{\partial q_1}{\partial x_i} = \sum_{I=1}^9 \sum_{k=1}^2 \frac{\partial N_I}{\partial \eta_k} \frac{\partial \eta_k}{\partial x_i} Q_{1I} \quad (3.10)$$

where N_I is the biquadratic shape function and Q_{1I} is the value of q_1 associated with the I th node of an element. Nodal values Q_{1I} are assigned in accordance with a smooth function. Numerical experiments have shown that the value of J is insensitive to the type of smooth function. Thus mesh design and convenience are the only considerations in selecting a smooth function. A detailed discussion of several aspects of the implementation of the domain representation of J , including candidate q_i functions, has been given by Shih et al. (1986).

3.5 Interaction Integral for Extracting Complex Stress Intensity Factors

Under the assumption of linear elasticity $G = J$, and therefore G has the line-integral representation

$$G = \int_{\Gamma} \left[\frac{1}{2} \sigma_{ik} \epsilon_{ik} \delta_{1j} - \sigma_{ij} \frac{\partial u_i}{\partial x_1} \right] n_j d\Gamma \quad (3.11)$$

The interaction energy release rate (see Appendix II, eq. (II.18)) is defined by

$$G_{\text{int}} = G_{\text{tot}} - G - G_{\text{aux}} \quad (3.12)$$

G_{tot} is the energy release rate of the total field (the actual field plus the auxiliary field) and G_{aux} is the energy release rate of the auxiliary field. It follows from (3.11) and (3.12) that

$$G_{\text{int}} = \int_{\Gamma} \left[\sigma_{ik} (\epsilon_{ik})_{\text{aux}} \delta_{1j} - \sigma_{ij} \left(\frac{\partial u_i}{\partial x_1} \right)_{\text{aux}} - (\sigma_{ij})_{\text{aux}} \frac{\partial u_i}{\partial x_1} \right] n_j d\Gamma \quad (3.13)$$

We have used the reciprocity theorem to make the connection

$$\frac{1}{2} \sigma_{ij}(\epsilon_{ij})_{aux} + \frac{1}{2}(\sigma_{ij})_{aux} \epsilon_{ij} = \sigma_{ij}(\epsilon_{ij})_{aux} . \quad (3.14)$$

By virtue of (3.12) and the path-independence of the integral in (3.11), the integral in (3.13) is also path-independent for an elastic homogeneous medium and for the bimaterial problem under consideration.

As mentioned in Section 3.3, it is more advantageous to work with domain representations in finite element computations. Using the weighting function q_1 discussed in Section 3.3, the domain representation of (3.13) is

$$G_{int} = \int_A \left\{ \left[-\sigma_{ik}(\epsilon_{ik})_{aux} \delta_{1j} + \sigma_{ij} \left[\frac{\partial u_i}{\partial x_1} \right]_{aux} + (\sigma_{ij})_{aux} \frac{\partial u_i}{\partial x_1} \right] \frac{\partial q_1}{\partial x_j} \right\} dA \quad (3.15)$$

where A is any annular domain surrounding the crack tip. Replacing the terms within the brackets [] in (3.9) by the terms within the brackets [] in (3.15), we have the finite element representation for G_{int} .

The method of extracting complex stress intensity factors will be explained using the particular boundary value problem under study. A more complete discussion is given in Appendix II. Let $(\sigma_{ik})_{aux}$, $(\epsilon_{ik})_{aux}$ and $(\partial u_i / \partial x_1)_{aux}$ be the singular fields for the deformable medium corresponding to unit value of the stress intensity factor K_1 (designated by k_1 in Appendix II). The singular stresses are given in Appendix I. The strains can be obtained using Hooke's law and $\partial u_2 / \partial x_1$ can be obtained, after some effort, from available solutions (e.g., Sih and Rice, 1964). The integral in (3.15) is evaluated using the actual numerical fields σ_{ij} and $\partial u_i / \partial x_1$ evaluated at the Gauss points, and the auxiliary fields (from Appendix I) also evaluated at the same Gauss points. Let $G_{int}^{(1)}$ denote the value of the interaction integral. As discussed in Appendix II (see eqs. (II.22) and (II.23)), the value of K_1 of the actual numerically determined fields for the problem at hand is given by

$$K_1 = \frac{2 \cosh^2 \pi \epsilon}{(1-\nu)/\mu} G_{int}^{(1)} . \quad (3.16)$$

Similarly, with the help of auxiliary singular fields appropriate to unit value of K_2 , $G_{int}^{(2)}$ is evaluated. The value of K_2 of the actual numerical fields is then given by

$$K_2 = \frac{2 \cosh^2 \pi \epsilon}{(1-\nu)/\mu} G_{int}^{(2)} \quad (3.17)$$

It may be noted that the method can also be applied to inclined crack and three-dimensional crack problems. In the case of isotropic homogeneous bodies, the usual K_I , K_{II} and K_{III} stress intensity factors are extracted from the numerical fields by using auxiliary fields appropriate to the isotropic homogeneous medium and the well-known relation between the energy release rate and K_I , K_{II} and K_{III} . Such an approach, using the line-integral (3.13) to calculate what is in effect G_{int} , has been employed by Yau et al. (1980), and Stern et al. (1976) for isotropic homogeneous media.

3.6 Computational Model

With reference to the geometry depicted in Fig. 3a, only the right half of deformable medium need be considered in the finite element analysis since the problem possesses reflective symmetry with respect to the vertical plane bisecting the crack. The half crack length is a , and the half width and height of the deformable slab is $100a$. The finite element model is constructed using 9-noded quadrilateral Lagrangian elements (see Fig. 3b) . We employ an arrangement of wedge-shaped 9-node elements in the immediate crack tip region - short of embedding the actual singularity fields into the elements, such an arrangement of elements contains sufficient degrees of freedom to reproduce the qualitative features of crack tip fields.

The wedge-shaped element has a radial length of $10^{-15}a$. The arrangement of wedge elements is surrounded by semi-circular strips of elements as shown in Fig. 3c. Each decade of radial length is spanned by four semi-circular strips of elements - thus the domain between $10^{-15}a$ and a is spanned by 60 strips of elements which are generated by a logarithmic scale.

Within each strip, the angular distance from 0 to π is spanned by 12 equally sized elements. The mesh for the domain $r \leq a$, as laid out in this manner, has 732 elements.

The domain beyond $r > a$, bounded by the remote boundaries and the symmetry plane, is modelled by 140 elements. All in all, there are 872 elements and 3639 nodes in the model. To test the adequacy of the mesh for the problem at hand, we carried out several elastic and elastic-plastic test calculations using the above mesh and a refined mesh which had twice as many elements. The results differed typically by less than 1 percent and we chose to use the coarser mesh to generate the results to be reported in the next section. The adequacy of the mesh design and the element type in conjunction with selective integration, and the accuracy of the domain representation for calculating J and the interaction integral will become evident in Section 4.

4. RESULTS

4.1 Mixed Mode Crack Tip Fields in Homogeneous Media

The plane strain elastic-plastic fields for the center cracked panel have been computed for the case where the upper and lower half materials are identical and are described by J_2 -deformation theory with power law hardening. In this case the near tip fields are essentially of the type originally derived by Hutchinson (1968a,b) and Rice and Rosengren (1968) for pure modes I and II and by Shih (1974) for mixed mode. Hereafter, they will be referred to as HRR fields. Application of the J -integral to the mixed mode small-scale yielding problem reveals that the dominant singularity governing the asymptotic behavior of the stresses, strains, and displacements near the crack tip has the form

$$\sigma_{ij} = \sigma_0 K^p r^{-1/(n+1)} \bar{\sigma}_{ij}(\theta; M^p, n), \quad \epsilon_{ij} = \frac{\alpha \sigma_0}{E} \left[K^p \right]^n r^{-n/(n+1)} \bar{\epsilon}_{ij}(\theta; M^p, n) \quad (4.1a,b)$$

$$u_i = \frac{\alpha \sigma_0}{E} \left[K^p \right]^n r^{1/(n+1)} \bar{u}_i(\theta; M^p, n), \quad \sigma_e = \sigma_0 K^p r^{-1/(n+1)} \bar{\sigma}_e(\theta; M^p, n). \quad (4.1c,d)$$

In the above expressions the dimensionless angular functions $\bar{\sigma}_{ij}$, $\bar{\epsilon}_{ij}$, and \bar{u}_i depend parametrically on the plastic mixity parameter, M^P , and the hardening exponent, n . The plastic mixity is defined as

$$M^P = \frac{2}{\pi} \tan^{-1} \left| \lim_{r \rightarrow 0} \frac{\sigma_{\theta\theta}(r, \theta=0)}{\sigma_{r\theta}(r, \theta=0)} \right| \quad (4.2)$$

such that $M^P = 1$ for pure mode I and $M^P = 0$ for pure mode II. The amplitude of the HRR singularity field, K^P (plastic stress intensity factor), is defined by Shih (1974) such that the angular distribution, $\bar{\sigma}_e$, attains a maximum value of unity. With this definition, K^P is related to the value of J by

$$J = \frac{\alpha \sigma_0^2}{E} I_n (K^P)^{n+1} . \quad (4.3)$$

The factor I_n depends on the degree of mixity, M^P , and n , and has been determined for a wide range of these parameters by Shih (1974). For our present purposes we find it convenient to rescale K^P by setting $I_n \equiv 1$.

For strictly linear elasticity, the mixity parameter can be reinterpreted as

$$M^P \rightarrow M^e \equiv \frac{2}{\pi} \tan^{-1} \left| \frac{K_I}{K_{II}} \right| . \quad (4.4)$$

For small scale yielding, where the stresses beyond the plastic zone are those of the elastic K -field, M^e is also defined by

$$M^e \equiv \frac{2}{\pi} \tan^{-1} \left| \frac{\sigma_{\theta\theta}(r^*, \theta=0)}{\sigma_{r\theta}(r^*, \theta=0)} \right| \quad (4.5)$$

where r^* is within the zone of dominance of the elastic field. In this case J is given by

$$J = \frac{(1-\nu^2)}{E} (K_I^2 + K_{II}^2) . \quad (4.6)$$

For the case of a finite crack in an infinite homogeneous plate, two types of loading are analyzed, one for which the elastic K field corresponds to pure mode I, and the other for which the mode is mixed. We define ψ as

$$\psi \equiv \tan^{-1} \left(\frac{\sigma_{12}^{\infty}}{\sigma_{22}^{\infty}} \right) = \tan^{-1} \left(\frac{K_{II}}{K_I} \right) = \pi/2(1-M^e) \quad (4.7)$$

Thus the two cases correspond to $\psi = 0^\circ$ and -30° . We chose to display the results for $\psi = -30^\circ$ because the mixed plastic field that develops under this loading bears noteworthy similarities to the field near the interface crack tip when the remote loading on the bimaterial plate is pure tension.

Figures 5a and 5b show distributions of stress ahead of the crack tip in a nonlinear homogeneous medium. The hoop stress, $\sigma_{\theta\theta}$, and effective stress, σ_e , along the central row of quadrature points in the first row of elements, $\theta = 7.5^\circ$, are shown for the cases where $n = 3$ and 10. The radial distances are normalized by r_p , the length of the plastic zone along $\theta = 0^\circ$. Note that the stresses plotted are the actual values computed at the Gauss points - we do not apply any smoothing to the data points in this and other figures in this paper.

In Fig. 5a $\ln(\text{stress}/\sigma_0)$ is plotted on the ordinate and the dotted line is the hoop stress according to the K field. The regions of elastic K-field dominance are indicated. Within the plastic zone the curves indeed take on the slopes $-1/4$ and $-1/11$ in accordance with (4.1a). In Fig. 5b the normalized stress, $\text{stress}/[\sigma_0[J/(\alpha\sigma_0\epsilon_0r)]^{1/(n+1)}]$, is plotted on the ordinate. The stress levels according to the HRR singularity fields (4.1a) for $n = 3$ and 10 are indicated. (These levels correspond to values of the dimensionless stress $\tilde{\sigma}_{\theta\theta}$ which are 1.26 and 2.16 respectively.) The normalized stresses are nearly invariant for $r < r_p$ and indicate fields that are entirely of pure mode I HRR form. Figures 6a and 6c show the angular distribution of normalized stress (defined as in Fig. 5b) deep inside the plastic zone, for $n = 3$ and 10, and $\psi = 0^\circ$. Figures 6b and 6d show the angular variations in stress for the mixed mode field corresponding to

$\psi = -30^\circ$. These normalized fields which are obtained from a full field analysis agree perfectly with the mixed mode asymptotic fields (Shih, 1974). One noteworthy feature of these fields is that the levels of normal stress, for a given overall value of the J-integral, are reduced for the mixed mode field. This is not only the case for the normal stress levels directly ahead of the crack, but is also true for the maximum values of stress over the full range of θ . Another interesting feature of the mixed mode solutions is the large shear stresses ahead of the crack tip.

Plastic zones determined from the analysis of the full boundary value problem are shown for these same values of n in Figs. 7a and 7b for pure mode I loading ($\psi = 0^\circ$) and mixed mode loading ($\psi = -30^\circ$). The plastic zones are essentially identical to those obtained by Shih (1974) based on an analysis of the small scale yielding boundary value problem. For the mixed mode case, the plastic zones are no longer symmetrical above and below the crack line and, for a fixed value of remote loading as measured by the value of J , extend further than for the pure mode I case (note the difference in the scale of the plots).

Contours of hydrostatic stress are shown in Figs. 7c and 7d. Here again, it is noteworthy that with pure mode I loading the contours are, as expected, symmetric about the crack line but become highly skewed under mixed mode loading. A feature of the hydrostatic stress field for the $n=10$ material is worth attention: at a fixed overall load level as measured by the value of J , the hydrostatic stress contour, $\sigma_h = \sigma_0$, for the mixed mode field extends further than the contour for the pure mode I field; however, the zone of high hydrostatic stress, $\sigma_h \geq 2\sigma_0$, is smaller under mixed mode field.

4.2 The Interface Crack in Linear Elastic Media

Figure 8 shows results for the near tip stress fields of the interface crack for $\nu = 0.3$. In Figs. 8a-8d normalized stresses are plotted in the form $\text{stress}/(JE/r)^{1/2}$. The analytically obtained asymptotic field (see Appendix I) is shown by the dotted line and

the essentially exact correspondence between it and our numerical solution is evident. At distances $r/a < 0.05$ from the crack tip, the differences between the numerical fields of the full boundary value problem of the center cracked plate and the analytic asymptotic fields are less than 5 percent (see Fig. 8a). This establishes a zone of dominance for the asymptotic linear elastic field.

Figure 8a, like Fig. 5, shows the radial distribution of stress along a ray connecting the central row of quadrature points in the elements along the bond line. Note that the field is of a strongly mixed nature characterized by large shear stresses. As noted in Section 2.1, the stresses begin to oscillate as the crack tip is approached and, $\sigma_{\theta\theta}$ first becomes compressive at $r/a \cong 10^{-9}$ at $\theta = 7.5^\circ$.

Figures 8b-8d show angular variations of stress at three radial distances from the crack tip. The strong dependence of the angular variations of the fields on the relative radial distance is evident.

To extract the stress intensity factors K_1 and K_2 from the numerical fields, the interaction integral (3.15) was evaluated on several semi-circular strips of elements with mean radii ranging from $10^{-14}a$ to a . The values of G_{int} obtained from the various strips differed only in the third or fourth significant digit. Specifically, for ν ranging from 0.0 to 0.499, the value for K_1 and K_2 , as determined by (3.16) and (3.17), agreed with the analytical solution given by Rice and Sih (1965) (see Fig. 2) to better than 2 significant digits. The excellent agreement attests to the quality of the numerical fields and the accuracy of the domain interaction integral (3.15) for uncoupling and evaluating stress intensity factors.

4.3 Small Scale Yielding for the Interface Crack Subject to Remote Tension

As discussed previously a characteristic feature of the asymptotic linear elastic solution is the increasingly rapid oscillations of the fields as the crack tip is approached. The relative crack face displacements, given by (2.5), imply wrinkling of the faces and

interpenetration near the tip of the crack. The finite element solutions accurately reproduce the oscillation in the stress field (see Fig. 8) and crack face penetration into the rigid substrate for distances greater than $10^{-15}a$ from the crack tip.

However, using the nonlinear model based on a power law hardening behavior, we find that at remote load levels which are a fraction of the yield stress, the crack face opens up smoothly. The finite element computations gave no indications that penetration into the rigid substrate would develop even at distances smaller than $10^{-15}a$. The stresses increase monotonically as we probe deeper into the plastic zone and there is no pattern that suggests that the stresses would reach a peak and then decrease as the distance within the plastic zone becomes vanishingly small. For one particular load level we repeated the entire calculation using a mesh which had twice as many elements. The numerical fields agreed to within two significant digits, strongly suggesting that fields at distances of $10^{-10}a$ to $10^{-15}a$ are accurately resolved by our computations.

At each stress level the value of J was extracted from the numerical fields using (3.9) and the 'plateau' q_1 function. The values of J evaluated on annular domains with mean radii ranging from $10^{-14}a$ to a generally agreed to within 3 significant digits. At stress levels where the maximum plastic zone size is much smaller than the crack length, the value of J agreed precisely with the analytical result of (2.16), viz.,

$$J = G = \frac{(1-\nu)/\mu}{4 \cosh^2 \pi \epsilon} (K_1^2 + K_2^2). \quad (4.8)$$

The essentially exact path-independence of the numerically evaluated J and the precise agreement with (4.8) under small scale yielding demonstrate the quality of the numerical solution and the accuracy of the domain method. The J values thus obtained are employed for the purpose of normalizing the fields to be discussed.

We choose to present results for a high hardening material ($n=3$) and a moderate to low hardening material ($n=10$) to reveal the effect of plasticity on the near tip fields. In particular, the behavior of the hoop stress ahead of the crack is shown in detail since

it is rather descriptive of the conditions at the interface and also plays an important role in fracture processes. Also, the variation of the hoop stress with radial distance is representative of the other stress components. In particular the hoop stress normalized by the remotely applied stress provides a direct indication of the intensification of the stress field. As before, the hoop stress at points on a radial line passing through the central row of Gauss points in the elements bonded to the interface ($\theta = 7.5^\circ$) is chosen for detailed examination. Since the distances under discussion range from $10^{-15}a$ to a it is necessary to plot $\log(r/a)$ on the abscissa. Over distances that differ by 15 orders of magnitude, the normalized hoop stress varies by several orders of magnitude, and in some cases is compressive. With the exception of a small interval where the hoop stress goes to zero and changes sign, the magnitude of the normalized hoop stress is much larger than unity within the distances under discussion. To grasp an overall picture of the behavior of the fields, we confine our attention to normalized stresses with magnitudes greater than unity. This permits the results to be presented in a rather compact and informative way. Specifically we take the log of $|\sigma_{\theta\theta}/\sigma^\infty|$ and to preserve the algebraic sign of the stress, the negative sign is appended. Accordingly, we plot $\text{sign}(\sigma_{\theta\theta})\log|\sigma_{\theta\theta}/\sigma^\infty|$.

The normalized stress determined by the finite element calculations for the strictly elastic material is plotted against normalized distance in Fig. 9a (see dashed-line curve). The break in the dashed-line curve near $\log(r/a) = -9.0$ corresponds to the stress changing from tension to compression. It should be noted that the position of the break in the dashed-line curve is independent of the remote tensile stress level. We now examine the behavior of the stress for the strongly hardening ($n=3$) nonlinear material. At the lowest load level considered, $\sigma^\infty/\sigma_0 = 2.0 \times 10^{-5}$, the plastic zone is confined to a distance of about $10^{-11}a$. While the stress is negative within the plastic zone, the slope of the curve becomes positive for $r/a < 10^{-14}$. At the next load level, $\sigma^\infty/\sigma_0 = 2.0 \times 10^{-4}$, the stress is positive over the entire distance studied, however, at the outer fringe of the

plastic zone, $10^{-9} < r/a < 10^{-8}$, the trend of the surrounding elastic field is felt. At distances well inside the plastic zone the hoop stress increases monotonically as the crack tip is approached. At a still higher load level, $\sigma^{\infty}/\sigma_0 = 6 \times 10^{-3}$, the hoop stress increases monotonically over the entire distance under discussion -- there is no trace of an oscillatory field.

The behavior of the hoop stress for a moderate to low hardening material is shown in Fig. 9b. For comparison purposes, the linear elastic result is again included. At the very low remote stress level $\sigma^{\infty}/\sigma_0 = 2.0 \times 10^{-5}$, the stress in the outer plastic zone is compressive in response, we note, to the compressive pressure of the surrounding elastic fields. Well within the plastic zone the stress is tensile. At the next remote stress level, $\sigma^{\infty}/\sigma_0 = 2.0 \times 10^{-4}$, the hoop stress in the outermost fringe of the plastic zone is weakly affected by the elastic fields. A short distance into the plastic zone, the hoop stress increases monotonically as the crack tip is approached. At the final load level, $\sigma^{\infty}/\sigma_0 = 6.0 \times 10^{-3}$, shown in the plot, there is no trace of any oscillatory field. (The solid line is terminated at $\log(r/a) = -12$ because we were unable to complete the calculations for the $n=10$ material at this load level using a mesh which could resolve fields at distances of $10^{-15}a$ from the crack tip.) We also note that, even at the largest remote stress level, the nonlinear crack tip region is surrounded by an annular zone, $10^{-5} < r/a < 10^{-2}$, in which the stresses are well approximated by the singular fields (2.13).

To develop a better understanding of the plastic fields we detail their angular distribution at two radial distances within the plastic zone and at three load levels: $\sigma^{\infty}/\sigma_0 = 2 \times 10^{-4}$, $\sigma^{\infty}/\sigma_0 = 6 \times 10^{-3}$ and $\sigma^{\infty}/\sigma_0 = 2 \times 10^{-1}$. We begin with the $n=3$ material. The length of the plastic zone as measured along the interface is denoted by r_p . The relative plastic zone size, r_p/a , corresponding to the three remote loads are 5.6×10^{-8} , 3.2×10^{-5} and 1.0×10^{-2} respectively. As mentioned previously, the asymptotic structure of the nonlinear crack tip fields has yet to be identified -- thus we do not have a definitive form with

which to organize the numerically calculated fields. For reasons which will be evident shortly, the stresses are normalized using an HRR structure; in particular, the normalized stresses are explicitly defined as:

$$\hat{\sigma}_{ij} = \frac{\sigma_{ij}/\sigma_0}{(J/\alpha\sigma_0\epsilon_0 r)^{1/(n+1)}} . \quad (4.9)$$

The angular distribution of the normalized stresses at a fixed relative distance $r/r_p = 1 \times 10^{-2}$, are shown in Figs. 10a, c and e for the three remote load levels. The angular fields deep inside the plastic zone, $r/r_p = 1.0 \times 10^{-6}$, are shown in Figs. 10b, d and e. It is clear from these plots that the fields are quite similar to the mixed mode HRR fields, for positive values of θ , shown in Fig. 6b. Specifically, within any given plastic zone the stress fields shift toward a mode I HRR type angular distribution as the distance moves deeper into the plastic zone (e.g. compare Figs. 10e and f). At a fixed distance relative to the plastic zone size, the angular fields also shift toward a mode I HRR type angular distribution as the remote load or the size of the plastic zone increases (e.g. compare Figs. 10c and e). Finally we point out that within the range of distances and loads examined, the normalized stresses are of order unity; the maximum value of the normalized hoop stress vary between 0.8 and 1.4.

It is instructive to examine the changes in the size and shape of the plastic zone as the remote load increases. To facilitate comparisons with the usual presentation of these plots (e.g. Shih, 1974), the distances are normalized by $JE/\{(1-\nu^2)\sigma_0^2\}$. The plastic zones at the three load levels are plotted in Fig. 11a, using these normalized distances

$$\bar{X} = x(1-\nu^2)\sigma_0^2/JE \quad \text{and} \quad \bar{Y} = y(1-\nu^2)\sigma_0^2/JE . \quad (4.10)$$

The relative size of the plastic zone decreases (when plotted on these non-dimensionalized axes) and changes over to a nearly mode I pattern as the remote load increases.

Hydrostatic stress contours for $\sigma_h = \sigma_0$ and $\sigma_h = 2.0\sigma_0$ are shown in Figs. 11b, c and d. The zone of high hydrostatic stress, $\sigma_h \geq 2\sigma_0$, increases in size as the field shifts towards a mode I distribution.

We detail the fields for the $n=10$ material at remote stress levels, σ^∞/σ_0 of 2×10^{-4} , 6×10^{-3} and 2×10^{-1} . The respective plastic zone sizes, r_p/a , are 8.2×10^{-8} , 4.2×10^{-5} and 1.2×10^{-2} . Plots of the angular fields at distances of $r/r_p = 1 \times 10^{-2}$ and 1×10^{-4} for the three remote stress levels are shown in Fig. 12. It is easily seen that the angular distribution of the plastic fields are nearly those of the mixed mode HRR type and that the fields deep inside the plastic zone (as in Fig. 12f) shift toward the mode I HRR distribution as shown in Fig. 6c.

Plastic zones corresponding to the three remote stress levels are shown in Fig. 13a. Again the shift towards a mode I pattern with increasing remote stress is easily seen. Hydrostatic stress contours are plotted in Figs. 13b, c and d; note the increase in the size of the zone of high hydrostatic stress, $\sigma_h \geq 1.7\sigma_0$, in Fig. 13d.

5. DISCUSSION

Our results suggest that a finite element method which uses selective integration (Malkus and Hughes, 1978; Hughes, 1980) and 9-node Lagrangian quadrilateral element is well suited for studying the complex nonlinear stress-strain fields near the tip of an interface crack. We find the method to be highly stable; the reduced integrations of volumetric fields using 4 quadrature points display no *hour glass* or other spurious modes. The method is easily programmed and, we note, lends itself to coding which is readily vectorized for supercomputers.

The full field numerical results presented in Section 4.3 indeed suggest that the near tip fields of the interface crack do not have a separable form of the type given by the HRR singularity (4.1). Nevertheless our small scale yielding solutions for the interface crack bear remarkable similarities to the fields for cracks in homogeneous

media subject to mixed mode loading. Furthermore within the distances that we have examined, the elastic-plastic fields do not exhibit any of the non-physical incompatible displacements and oscillatory stresses that are characteristic of the small strain linear elastic solutions. We discuss these features in turn.

For the boundary value problem at hand we note that, under small scale yielding conditions,

$$J = \frac{(\sigma_{22}^{\infty})^2 \pi a (1+4\epsilon^2)}{4 \cosh^2 \pi \epsilon} (1-\nu)/\mu. \quad (5.1)$$

If J_0 is the value of J for a similar crack in a homogeneous plate then, for a fixed remote stress σ_{22}^{∞} ,

$$\frac{J}{J_0} = \frac{(1+4\epsilon^2)}{2 \cosh^2 \pi \epsilon}. \quad (5.2)$$

For the case of the crack on a rigid substrate with $\nu = 0.3$ in the deformable medium, $\epsilon \cong 0.0935$ as already noted, and $J/J_0 \cong 0.475$. We now recall the distributions in each of Figs. 6, 10 and 12 where the stresses are normalized by the quantity $q = \sigma_0 [J/(\alpha \sigma_0 \epsilon_0 r)]^{1/(n+1)}$. With this perspective it is clear that for a fixed intensity of remote loading, as measured by σ_{22}^{∞} , the stresses near the tip are generally lower for the interface crack than those for the crack in a homogeneous media. However, at a given value of J the stresses near the tip of the interface crack are generally higher; at larger distances from the crack tip, the stresses are comparable or lower than those for the homogeneous media. For example, the maximum value of $(\sigma_{\theta\theta}/q)$ in a homogeneous medium, under mixed mode loading corresponding to $\psi = -30^\circ$, is $\sigma_{\theta\theta}/q \cong 1.1$ when $n=3$ and $\sigma_{\theta\theta}/q \cong 1.7$ when $n=10$. For the interface crack, the maximum stress levels, at each radial distance, depend on distance and remote stress level. At the normalized distance $r/r_p = 1.0 \times 10^{-2}$, $\sigma_{\theta\theta}/q \cong 0.9, 1.1,$ and 1.25 for the three remote stress levels plotted in Fig. 10 $n=3$. At the distance $r/r_p = 1.0 \times 10^{-6}$, $\sigma_{\theta\theta}/q \cong 1.2, 1.35,$ and 1.45

which are considerably larger than those for a crack in a homogeneous medium. The same trends hold for $n=10$. It should be noted that the angular distribution of the stresses for the interface crack can be quite different from those for the crack in a homogeneous medium. An important difference is the large shear stresses and strains that develop near the bond line of an interface crack despite the tensile nature of the remote stresses.

Another intriguing feature of the stress fields of the interface crack is how the degree of mixity of the near tip fields changes with the extent of plasticity. For example, comparing Figs. 12 and 6c and 6d for $n=10$, it may be seen that as the remote stress level increases, and as the positions examined are closer to the crack tip, the field more nearly resembles that of a pure mode I HRR field. Indeed, near tip fields for remote stress $\sigma^\infty/\sigma_0 > 0.2$ are essentially of pure mode I distribution. A discussion of these fields is deferred to a later paper. At lower stress levels, and at distances more remote from the crack tip, the field has features similar to the homogeneous mixed mode, for example that for $\psi = -30^\circ$.

As noted in Sections 2 and 4, the small strain linear elastic asymptotic field for an interface crack is characterized by displacement incompatibilities and oscillatory stresses. In Section 2 it was noted that under combined remote tension and shear, the regions ahead of the crack where the stresses oscillate can be significant fractions of the crack length, thus rendering the solutions physically unacceptable. Within the nonlinear theory of plane stress Knowles and Sternberg (1983) have carried out an elegant asymptotic analysis of an interface crack between two neo-Hookean sheets. Their asymptotic fields, based on nonlinear kinematics and a linear relation between the Cauchy shear stress and shear displacement, are free of oscillatory singularities; they also found that the crack opens smoothly near its ends. Our full field solutions show that, even within the framework of linearized kinematics, accounting for nonlinear material behavior effectively precludes incompatible displacements and stress oscillations. This is true not

only for the case of remotely applied pure tension but, as we have noted, for the more general case of combined remote tension and shear. To demonstrate this we analyzed the case where $\sigma_{22}^{\infty} > 0$ and $\sigma_{12}^{\infty} = -2\sigma_{22}^{\infty}$, or as described in connection with (2.11) and (2.12) where $\lambda \cong -58.7^{\circ}$. The results shown in Figs. 14 and 15 were obtained by performing a *boundary layer*, small scale yielding analysis in which the stresses, given by the asymptotic field in Appendix I, were imposed at a distance which is large compared to the plastic zone size. The stress intensities for this case were prescribed as $K_1 = \sigma_{22}^{\infty}(1-4\epsilon)\sqrt{\pi a}$ and $K_2 = \sigma_{22}^{\infty}(2+2\epsilon)\sqrt{\pi a}$ with σ_{22}^{∞} taken to be the scalar stress variable (see Fig. 2c).

Figure 14a shows the linear elastic results for the stress variations along a radial line at $\theta = 7.5^{\circ}$ for the combined remote tension and shear loading. It may be recalled from Section 2 that on the bond line $\sigma_{\theta\theta}$ is compressive at $r/a \cong 2 \times 10^{-3}$. At $\theta = 7.5^{\circ}$, $\sigma_{\theta\theta}$ is compressive at $r/a \cong 3 \times 10^{-4}$. Figure 14b shows the radial distributions of stress, again along the central row of quadrature points at $\theta = 7.5^{\circ}$, for a nonlinear material with $n=3$ and for three remote stress levels. In the plot the hoop stress $\sigma_{\theta\theta}$ is normalized by σ_{22}^{∞} which is labelled as σ^{∞} . Note that with combined loading of this sort, that is with $\sigma_{12}^{\infty} < 0$, larger remote levels of σ_{22}^{∞} , as compared to the cases dominated by remote tension, are required to 'open the crack' and produce monotonically increasing stresses as the crack tip is approached. Nevertheless even at the rather low remote stress level of $\sigma_{22}^{\infty}/\sigma_0 = 1.0 \times 10^{-1}$ oscillatory stresses and overlapping of the crack faces are precluded in a high hardening material. In a moderate to low hardening material, the oscillatory fields are precluded at substantially lower remote tensile stresses. Indeed, even at rather low stress levels, the characteristics of the plastic fields (which are totally different from those predicted by linear elasticity) prevail over significant length scales.

Figure 15 shows the angular distribution of stresses at six radial distances within the plastic zone for the remote loading corresponding to $\sigma_{22}^{\infty}/\sigma_0 = 1.0 \times 10^{-1}$ and $\sigma_{12}^{\infty}/\sigma_0 = -2.0 \times 10^{-1}$. For this load level, $r_p/a \cong 5.0 \times 10^{-2}$ which is also the maximum

extent of the plastic zone. A remarkable feature of these fields is the gradual shift towards a mode I like HRR field as the distance r/r_p becomes vanishingly small despite the relatively large remote shear stresses. This trend can be clearly seen by comparing the angular variations of the fields in Fig. 15 to the fields in Fig. 10 which are associated with pure remote tension.

Despite the pathological nature of the linear elastic singular fields, we must point out that there is a finite annular region where the elastic singular fields (2.13) is a good approximation of the full field solution as can be seen in Fig. 9 and Fig. 14. It is in this more restricted sense, that we speak of small scale yielding; *in the present context the term does not imply self-similar growth of the plastic zone.* In a sequel to this paper, the near tip fields for an isolated crack and collinear arrays of cracks under contained yielding and essentially fully yielded conditions will be presented and implications for interface fracture will be discussed.

APPENDIX I

Singular Fields Near the Tip of an Interface Crack

As noted in the text, the asymptotic crack tip fields for the case of linear isotropic media take the form

$$\sigma_{ij} = \sum_{\alpha=1}^2 \frac{K_{\alpha}}{\sqrt{2\pi r}} g_{ij}^{(\alpha)} [\theta, \epsilon \ln(r/2a); \epsilon] . \quad (I.1)$$

The stress intensity factors, K_{α} , in (I.1) were defined in (2.1) with examples given in Fig. 2. For the bimaterial geometries shown in Fig. 2 the full form of the singular field in region 1 is given by (I.1) with the $g_{ij}^{(\alpha)}$ defined as follows. Let (ij) denote the polar indices (r θ) and define A as

$$A = \frac{1}{2 \cosh(\pi\epsilon)} . \quad (I.2)$$

Then

$$g_{rr}^{(1)} = A \left[e^{-\epsilon(\pi-\theta)} \left\{ 3 \cos(\theta/2 + \epsilon \ln(r/2a)) + 2\epsilon \sin\theta \cos(\theta/2 - \epsilon \ln(r/2a)) \right. \right. \\ \left. \left. - \sin\theta \sin(\theta/2 - \epsilon \ln(r/2a)) \right\} \right. \\ \left. - e^{\epsilon(\pi-\theta)} \cos(3\theta/2 + \epsilon \ln(r/2a)) \right] , \quad (I.3)$$

$$g_{rr}^{(2)} = A \left[e^{-\epsilon(\pi-\theta)} \left\{ -3 \sin(\theta/2 + \epsilon \ln(r/2a)) + 2\epsilon \sin\theta \sin(\theta/2 - \epsilon \ln(r/2a)) \right. \right. \\ \left. \left. + \sin\theta \cos(\theta/2 - \epsilon \ln(r/2a)) \right\} \right. \\ \left. + e^{\epsilon(\pi-\theta)} \sin(3\theta/2 + \epsilon \ln(r/2a)) \right] , \quad (I.4)$$

$$g_{\theta\theta}^{(1)} = A \left[e^{-\epsilon(\pi-\theta)} \left\{ \cos(\theta/2 + \epsilon \ln(r/2a)) - 2\epsilon \sin\theta \cos(\theta/2 - \epsilon \ln(r/2a)) \right. \right. \\ \left. \left. + \sin\theta \sin(\theta/2 - \epsilon \ln(r/2a)) \right\} \right. \\ \left. + e^{\epsilon(\pi-\theta)} \cos(3\theta/2 + \epsilon \ln(r/2a)) \right] , \quad (I.5)$$

$$g_{\theta\theta}^{(2)} = A \left[e^{-\epsilon(\pi-\theta)} \left\{ -\sin(\theta/2 + \epsilon \ln(r/2a)) - 2\epsilon \sin\theta \sin(\theta/2 - \epsilon \ln(r/2a)) \right. \right. \\ \left. \left. - \sin\theta \cos(\theta/2 - \epsilon \ln(r/2a)) \right\} \right. \\ \left. - e^{\epsilon(\pi-\theta)} \sin(3\theta/2 + \epsilon \ln(r/2a)) \right] , \quad (I.6)$$

$$g_{r\theta}^{(1)} = A \left[e^{-\epsilon(\pi-\theta)} \left\{ \sin(\theta/2 + \epsilon \ln(r/2a)) - 2\epsilon \sin\theta \sin(\theta/2 - \epsilon \ln(r/2a)) \right. \right. \\ \left. \left. - \sin\theta \cos(\theta/2 - \epsilon \ln(r/2a)) \right\} \right. \\ \left. + e^{\epsilon(\pi-\theta)} \sin(3\theta/2 + \epsilon \ln(r/2a)) \right] , \quad (I.7)$$

$$g_{r\theta}^{(2)} = A \left[e^{-\epsilon(\pi-\theta)} \left\{ \cos(\theta/2 + \epsilon \ln(r/2a)) + 2\epsilon \sin\theta \cos(\theta/2 - \epsilon \ln(r/2a)) \right. \right. \\ \left. \left. - \sin\theta \sin(\theta/2 - \epsilon \ln(r/2a)) \right\} \right. \\ \left. + e^{\epsilon(\pi-\theta)} \cos(3\theta/2 + \epsilon \ln(r/2a)) \right] . \quad (I.8)$$

These asymptotic fields can easily be rearranged into the form given by Sih and Rice (1964) by redefining K as their k as described in Section 2.

APPENDIX II

Crack Field Mode Interaction

In this section we describe a method for calculating the individual stress modes for a crack subjected to mixed mode loading. The method is applicable to cracks in isotropic or anisotropic media. Our method is motivated by Eshelby's (1956, 1961) notion of *interaction forces* and, in the present context, this means an *interaction energy release rate*, G_{int} . To begin, consider the field of a finite size crack (such as shown in Fig. 1) in an arbitrary anisotropic but homogeneous elastic media. The remote tension loading, σ_{22}^{∞} , is augmented with the remote shear stress σ_{12}^{∞} (as depicted in Fig. 2c). Let x_1, x_2 be the Cartesian coordinates such that the line crack lies along the x_1 -axis over the region $-a \leq x_1 \leq a$. Along the crack line

$$\sigma_{i2} = \sigma_{i2}^{\infty} \frac{|x_1|}{(x_1^2 - a^2)^{\frac{1}{2}}}; \quad |x_1| > a, \quad x_2 = 0, \quad i = 1, 2, 3. \quad (II.1)$$

At a vanishingly small distance from the right crack tip and, with ξ defined as in the text (Fig. 1),

$$\sigma_{i2} = \sigma_{i2}^{\infty} \left[\frac{a}{2\xi} \right]^{\frac{1}{2}}, \quad \xi > a, \quad x_2 = 0. \quad (II.2)$$

Note that on the crack line the tractions are independent of elastic constants and are essentially set by static equilibrium (Barnett and Asaro, 1972).

In homogeneous media the notion of stress intensity factors is tied to the symmetry in the stress fields which are expressed in the form (r, θ are polar coordinates centered on the crack tip)

$$\sigma_{ij} = \sum_{\alpha=I}^{III} K_{\alpha} / (2\pi r)^{\frac{1}{2}} f_{ij}^{(\alpha)}(\theta) \quad (II.3)$$

where

$$f_{22}^I(\theta=0) = 1, \quad f_{12}^I(0) = 0 = f_{32}^I(0) \quad (\text{II.4}_1)$$

$$f_{12}^{II}(\theta=0) = 1, \quad f_{22}^{II}(0) = 0 = f_{32}^{II}(0) \quad (\text{II.4}_2)$$

and

$$f_{32}^{III}(\theta=0) = 1, \quad f_{22}^{III}(0) = 0 = f_{12}^{III}(0) \quad (\text{II.4}_3)$$

For the problem at hand then,

$$K_I = \sigma_{22}^\infty \sqrt{a\pi}, \quad K_{II} = \sigma_{12}^\infty \sqrt{a\pi}, \quad K_{III} = \sigma_{32}^\infty \sqrt{a\pi}. \quad (\text{II.5}_{1,2,3})$$

The displacement fields will not possess such simple symmetries, and again for the problem at hand we note that the jump in displacement across the crack tip is given by Barnett and Asaro (1972) as

$$\Delta u_i = B_{ij}^{-1} \sigma_{j2} \sqrt{a/\pi} \sqrt{x/2\pi}, \quad |x| \leq a \quad (\text{II.6})$$

where B^{-1} is the inverse of the so-called prelogarithmic energy factor matrix, B .

For plane strain we can define a *stress intensity vector* with components

$$\mathbf{K} = \{K_{II}, K_I\} \quad (\text{II.7})$$

such that the crack traction vector and the displacement jumps on the crack line

$$\mathbf{t} = \{\sigma_{12}, \sigma_{22}\} \quad (\text{II.8})$$

and

$$\Delta \mathbf{u} = \{\Delta u_1, \Delta u_2\} \quad (\text{II.9})$$

are given by

$$\mathbf{t} = \frac{1}{\sqrt{2\pi x}} \mathbf{K}, \quad x > a \quad (\text{II.10})$$

and

$$\Delta \mathbf{u} = \frac{1}{\pi} B^{-1} \cdot \mathbf{K} \sqrt{x/2\pi}, \quad |x| < a. \quad (\text{II.11})$$

The energy release rate can be calculated from the virtual work integral of (2.14) and is given by Barnett and Asaro (1972) as

$$G = \frac{1}{8\pi} K_{\alpha} B_{\alpha\beta}^{-1} K_{\beta} \quad (\text{II.12})$$

where the indices α, β can be interpreted such that 1 is identified with II and 2 with I. Note that for isotropic media B is diagonal, with components

$$B_{11} = B_{22} = \frac{\mu}{4\pi(1-\nu)} \quad \text{and} \quad B_{33} = \frac{\mu}{4\pi}, \quad (\text{II.13})$$

and the usual expressions for t , Δu , and G are recovered, i.e.,

$$G = \frac{(1-\nu)}{2\mu} [K_I^2 + K_{II}^2] + \frac{1}{2\mu} K_{III}^2 \quad (\text{II.14})$$

Stress mode decoupling in a given mixed mode stress field is accomplished through computation of what might be referred to as an *interaction energy release rate*. To appreciate the procedure, the details of calculating the K_I component of a total crack tip field are illustrated.

We first note that for the actual (mixed mode) crack field the crack extension force is given by

$$G = \frac{1}{8\pi} \left[K_I B_{11}^{-1} K_I + 2K_I B_{12}^{-1} K_2 + 2K_I B_{13}^{-1} K_3 + \right. \\ \left. (\text{terms not involving } K_I) \right]. \quad (\text{II.15})$$

Now suppose that an auxiliary pure mode I field, of intensity k_1 , is superimposed on the actual field and the crack extension force again computed; the result is

$$G_{\text{tot}} = \frac{1}{8\pi} \left[(K_I + k_1) B_{11}^{-1} (K_I + k_1) + 2(K_I + k_1) B_{12}^{-1} K_I \right. \\ \left. + 2(K_I + k_1) B_{13}^{-1} K_3 + (\text{terms not involving } K_I \text{ or } k_1) \right]. \quad (\text{II.16})$$

The auxiliary field itself has the energy release rate

$$G_{\text{aux}} = \frac{1}{8\pi} k_1 B_{11}^{-1} k_1 . \quad (\text{II.17})$$

From the above relations we can define an interaction extension force as

$$G_{\text{int}} = G_{\text{tot}} - G - G_{\text{aux}} = \frac{1}{8\pi} \left[2k_1 B_{11}^{-1} K_1 + 2k_1 B_{12}^{-1} K_1 + 2k_1 B_{13}^{-1} K_3 \right]. \quad (\text{II.18})$$

All three energy release rates, G , G_{tot} , and G_{aux} , including G_{int} itself, are computable from either line or domain integrals as explained in Sections 3.3 to 3.5. When the above calculations are performed for the other two modes a simple linear system of equations of the

form

$$G_{\text{int}}^{(\alpha)} = \frac{1}{4\pi} k_{\alpha} B_{\alpha\beta}^{-1} K_{\beta} , \quad (\text{no sum on } \alpha = 1, 2, 3) \quad (\text{II.19})$$

results which may easily be solved for the K_{β} ; when the k_{α} are assigned unit values the solution for the K_{β} are

$$K_{\alpha} = 4\pi B_{\alpha\beta} G_{\text{int}}^{(s)} . \quad (\text{II.20})$$

It may be noted that G_{int} is readily evaluated with high precision via the domain integrals described in Section 3.5.

A completely analogous procedure can be applied to evaluate the respective intensities of the two stress modes K_1 and K_2 for the present interface crack being investigated. For plane strain we note by (2.16) that, if G is written in the form

$$G = K_{\alpha} B_{\alpha\beta}^{-1} K_{\beta} , \quad (\text{II.21})$$

that B is diagonal with the nonzero components

$$B_{11}^{-1} = B_{22}^{-1} = B^{-1} = \{(1-\nu_1)/\mu_1\}/(4\cosh^2\pi\epsilon) . \quad (\text{II.22})$$

Once the two $G_{\text{int}}^{(\alpha)}$ are evaluated, the two stress intensities are determined from

$$K_{\alpha} = \frac{1}{2} B G_{\text{int}}^{(\alpha)} . \quad (\text{II.23})$$

ACKNOWLEDGEMENTS

We are grateful to Margaret Symington who made many helpful suggestions in the presentation of the material. This investigation is supported by the Office of Naval Research through ONR Grant "Mechanics of Interface Cracks." The computations reported on here were performed in the Computational Mechanics Facility at Brown University and at the Supercomputer Facility at the U.S. Naval Research Laboratory.

REFERENCES

- Barnett, D. M. and Asaro, R. J., 1972, "The Fracture Mechanics of Slit-like Cracks in Anisotropic Elastic Media," *Journal of the Mechanics and Physics of Solids*, Vol. 20, pp. 353-366.
- Belytschko, T. and Tsay, C. S., 1983, "A Stabilization Procedure for the Quadrilateral Plate Element with One-Point Quadrature," *International Journal for Numerical Methods in Engineering*, Vol. 19, pp. 405-419.
- deLorenzi, H. G., 1982, "On Energy Release Rate and the J-integral for 3-D Crack Configurations," *International Journal of Fracture*, Vol. 19, pp. 183-193.
- England, A. H., 1965, "A Crack Between Dissimilar Media," *Journal of Applied Mechanics*, Vol. 32, pp. 400-402.
- Erdogan, F., 1963, "Stress Distribution in a Nonhomogeneous Elastic Plane with Cracks," *Journal of Applied Mechanics*, Vol. 30, pp. 232-236.
- Erdogan, F., 1965, "Stress Distribution in Bonded Dissimilar Materials with Cracks," *Journal of Applied Mechanics*, Vol. 32, pp. 403-410.
- Eshelby J. D., 1956, "The Continuum Theory of Lattice Defects," *Solid State Physics*, (edited by Seitz and Turnbull), Vol. 3, pp. 79-144.
- Eshelby, J. D., 1961, "Elastic Inclusions and Inhomogeneities," *Progress in Solid Mechanics*, (edited by Sneddon & Hill) Vol. 2, pp. 87-140.
- Hellen, T. K., 1975, "On the Method of Virtual Crack Extension," *International Journal for Numerical Methods in Engineering*, Vol. 9, pp. 187-207.
- Hughes, T. J. R., 1980, "Generalization of Selective Integration Procedures to Anisotropic and Nonlinear Materials," *International Journal for Numerical Methods in Engineering*, Vol. 15, pp. 1413-1418.
- Hutchinson, J. W., 1968a, "Singular Behavior at the End of a Tensile Crack in a Hardening Material," *Journal of the Mechanics and Physics of Solids*, Vol. 16, pp. 13-31.
- Hutchinson, J. W., 1968b, "Plastic Stress and Strain Fields at a Crack Tip," *Journal of the Mechanics and Physics of Solids*, Vol. 16, pp. 337-347.
- Hutchinson, J. W., 1983, "Fundamentals of the Phenomenological Theory of Nonlinear Fracture Mechanics," *Journal of Applied Mechanics*, Vol. 50, pp. 1042-1051.
- Knowles, J. K. and Sternberg, E., 1983, "Large Deformations Near a Tip of an Interface-Crack Between Two Neo-Hookean Sheets," *Journal of Elasticity*, Vol. 13, pp. 257-293.
- Li, F. Z., Shih, C. F. and Needleman, A., 1985, "A Comparison of Methods for Calculating Energy Release Rates," *Engineering Fracture Mechanics*, Vol. 21, pp. 405-421.
- Malkus, D. S. and Hughes, T. J. R., 1978, "Mixed Finite Element Methods - Reduced and Selective Integration Techniques: A Unification of Concepts," *Computer Methods in Applied Mechanics and Engineering*, Vol. 15, pp. 63-81.

- Moran, B., and Shih, C. F., 1986, "Crack Tip and Associated Domain Integrals from Momentum and Energy Balance," to appear in *Engineering Fracture Mechanics*.
- Nagtegaal, J. C., Parks, D. M. and Rice, J. R., 1974, "On Numerically Accurate Finite Element Solutions in the Fully Plastic Range," *Computer Methods in Applied Mechanics and Engineering*, Vol. 4, pp. 153-178.
- Parks, D. M., 1977, "The Virtual Crack Extension Method for Nonlinear Material Behavior," *Computer Methods in Applied Mechanics and Engineering*, Vol. 12, pp. 353-364.
- Rice, J. R. and Sih, G. C., 1965, "Plane Problems of Cracks in Dissimilar Media," *Journal of Applied Mechanics*, Vol. 32, pp. 418-423.
- Rice, J. R. and Rosengren, G. F., 1968, "Plane Strain Deformation Near a Crack Tip in a Power Law Hardening Material," *Journal of the Mechanics and Physics of Solids*, Vol 16, pp. 1-12.
- Rice, J. R., 1968, "A Path Independent Integral and the Approximate Analysis of Strain Concentration by Notches and Cracks," *Journal of Applied Mechanics*, Vol. 35, pp. 379-386.
- Shih, C. F., 1974, "Small-Scale Yielding Analysis of Mixed Mode Plane-Strain Crack Problems," in *Fracture Analysis*, ASTM STP 560, pp 187-210.
- Shih, C. F. and Needleman, A., 1984, "Fully Plastic Crack Problems," Parts I and II, *Journal of Applied Mechanics*, Vol. 51, pp. 48-56, pp. 57-64.
- Shih, C. F., Moran, B. and Nakamura, T., 1986, "Energy Release Rate Along a Three-Dimensional Crack Front in a Thermally Stressed Body," *International Journal of Fracture*, Vol. 30, pp. 79-102.
- Sih, G. C. and Rice, J. R., 1964, "The Bending of Plates of Dissimilar Materials with Cracks," *Journal of Applied Mechanics*, Vol. 31, pp. 477-482.
- Stern, M., Becker, E. B. and Dunham, R. S., 1976, "A Contour Integral Computation of Mixed Mode Stress Intensity Factors," *International Journal of Fracture*, Vol. 12, pp. 359-368.
- Williams, M. L., 1959, "The Stresses Around a Fault or Crack in Dissimilar Media," *Bulletin of the Seismological Society of America*, Vol. 49, pp. 199-204.
- Willis, J. R., 1971, "Fracture Mechanics of Interfacial Cracks," *Journal of the Mechanics and Physics of Solids*, Vol. 19, pp. 353-368.
- Yau, J. F., Wang, S. S. and Corten, H. T., 1980, "A Mixed-Mode Crack Analysis of Isotropic Solids Using Conservation Laws of Elasticity," *Journal of Applied Mechanics*, Vol. 47, pp. 335-341.
- Zienkiewicz, O. C., 1977, *The Finite Element Method*, 3rd Edition, McGraw-Hill, London.

FIGURE CAPTIONS

- Figure 1: Interface crack between two bonded dissimilar materials.
- Figure 2: Stress intensity factors for three crack geometries.
- Figure 3: (a) Interface crack between deformable medium and rigid substrate. (b) Finite element mesh of right half of deformable medium. (c) Arrangement of elements at crack tip.
- Figure 4: Conventions for domain J. Domain A is enclosed by Γ , C_+ , C_- and C_0 . Unit normal $m_j = n_j$ on C_0 and $m_j = -n_j$ on Γ .
- Figure 5: (a) Stresses ahead of crack tip in homogeneous medium; the zone of K dominance is indicated. (b) Normalized stress versus distance normalized by plastic zone size.
- Figure 6: Angular variations of normalized stresses in homogeneous medium subject to pure mode I and mixed mode loadings; (a) and (b) $n=3$ material; (c) and (d) $n=10$ material.
- Figure 7: (a) and (b) Plastic zones in homogeneous medium subject to mode I and mixed mode loadings; (c) and (d) Hydrostatic stress contours corresponding to mode I and mixed mode loadings.
- Figure 8: (a) Normalized stresses (from linear elastic calculations, $n=1$) near the bond line versus log distance; the asymptotic stresses are included. (b), (c) and (d) Angular variations of normalized stresses at three radial distances.
- Figure 9: Plots of log of normalized hoop stress (near the bond line) against log of normalized distance for the interface crack; (a) $n=3$ material, (b) $n=10$ material. The elastic ($n=1$) result is included.
- Figure 10: Plots of angular variations of normalized stresses for the interface crack with $n=3$ at two distances within the plastic zone and for three remote stress levels.
- Figure 11: (a) Plastic zones for the interface crack with $n=3$ for three remote stress levels. (b), (c) and (d) Hydrostatic stress contours for three remote stress levels. The normalized distances are defined as $\bar{X} = x(1-\nu^2)\sigma_0^2/JE$ and $\bar{Y} = y(1-\nu^2)\sigma_0^2/JE$.
- Figure 12: Plots of angular variations of normalized stresses for the interface crack with $n=10$ at two distances within the plastic zone and for three remote stress levels.
- Figure 13: (a) Plastic zones for the interface crack with $n=10$ for three remote stress levels. (b), (c) and (d) Hydrostatic stress contours for three remote stress levels. The normalized distances are defined as $\bar{X} = x(1-\nu^2)\sigma_0^2/JE$ and $\bar{Y} = y(1-\nu^2)\sigma_0^2/JE$.

Figure 14: Hoop stress near the bond line due to combined remote tension and shear. (a) Normalized stresses from linear elastic calculations ($n=1$); the asymptotic stresses are included. (b) Normalized hoop stress for nonlinear material behavior with $n=3$. The elastic ($n=1$) result is included.

Figure 15: Plots of angular variations of normalized stresses for the interface crack with $n=3$ at six distances within the plastic zone for remote stresses given by $\sigma_{22}^{\infty}/\sigma_0 = 0.1$ and $\sigma_{12}^{\infty}/\sigma_0 = -0.2$.

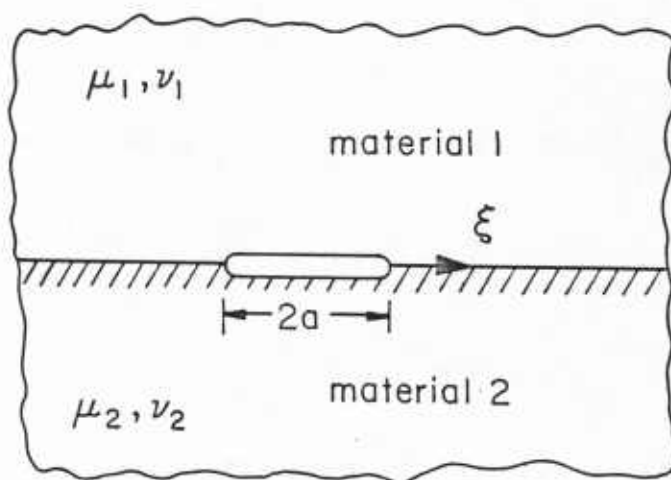


FIG. 1

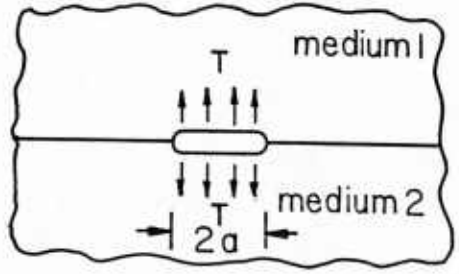
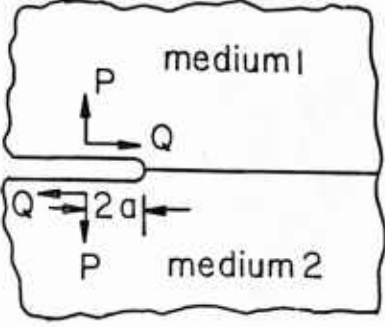
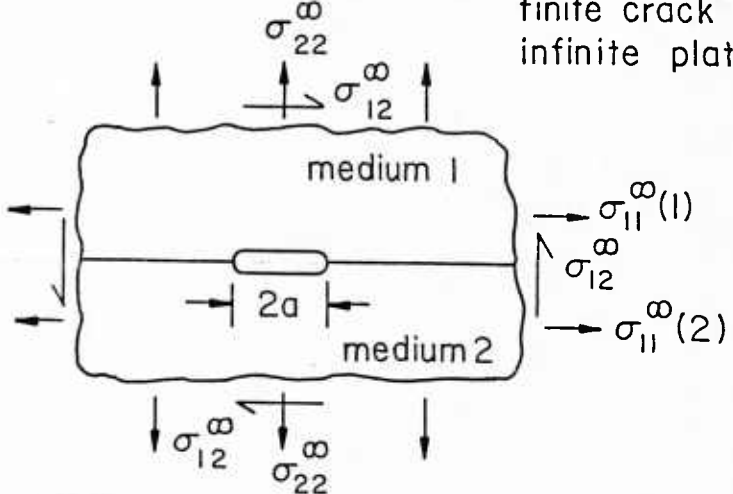
Ref.	Crack Configuration	$K=K_1+iK_2$
England, 1965	 <p style="text-align: center;">uniform pressure on crack face</p> <p style="text-align: right;">(a)</p>	$K=T\sqrt{\pi a}\{1+i2\epsilon\}$
Rice and Sih, 1965	 <p style="text-align: center;">semi-infinite crack subject to point loads</p> <p style="text-align: right;">(b)</p>	$K=\frac{P+iQ}{\sqrt{\pi a}}\cosh \pi \epsilon$
Rice and Sih, 1965	 <p style="text-align: center;">finite crack in infinite plate</p> <p style="text-align: right;">(c)</p>	$K=\{(\sigma_{22}^{\infty}-2\sigma_{12}^{\infty}\epsilon)+i(\sigma_{12}^{\infty}+2\epsilon\sigma_{22}^{\infty})\}\sqrt{\pi a}$

FIG. 2

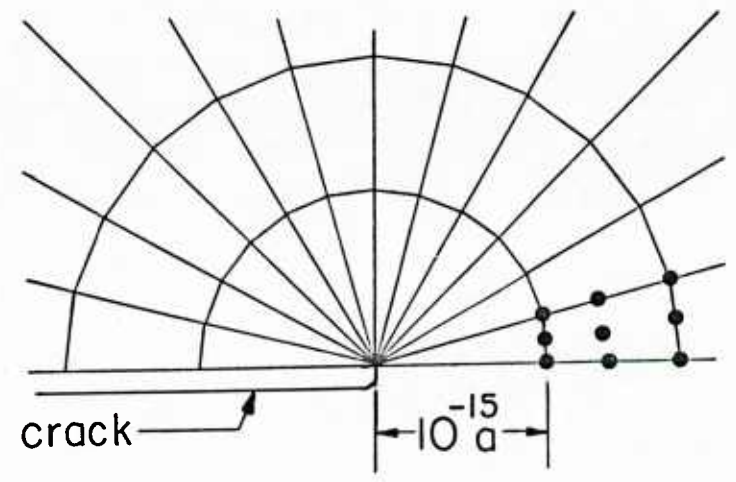
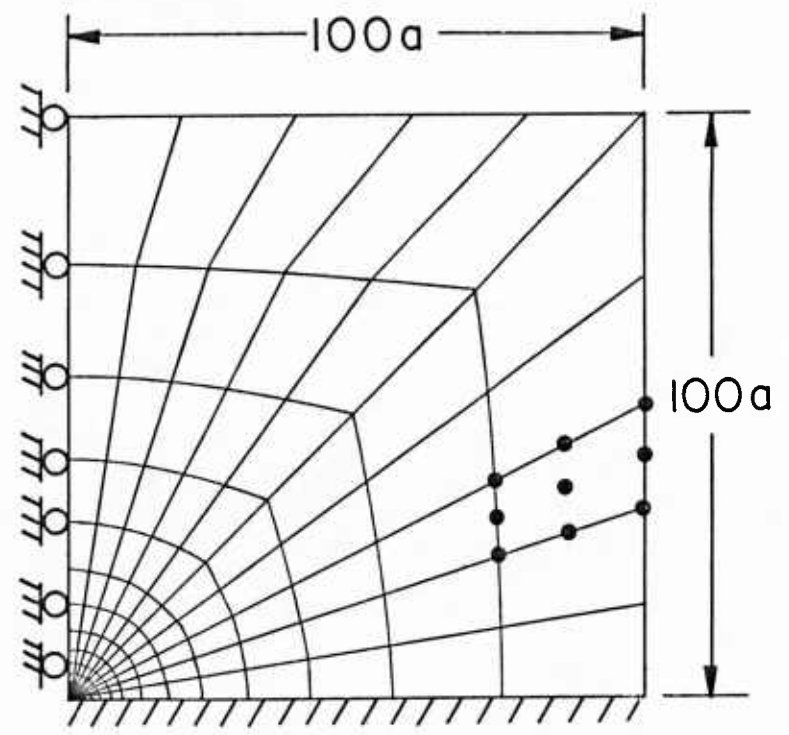
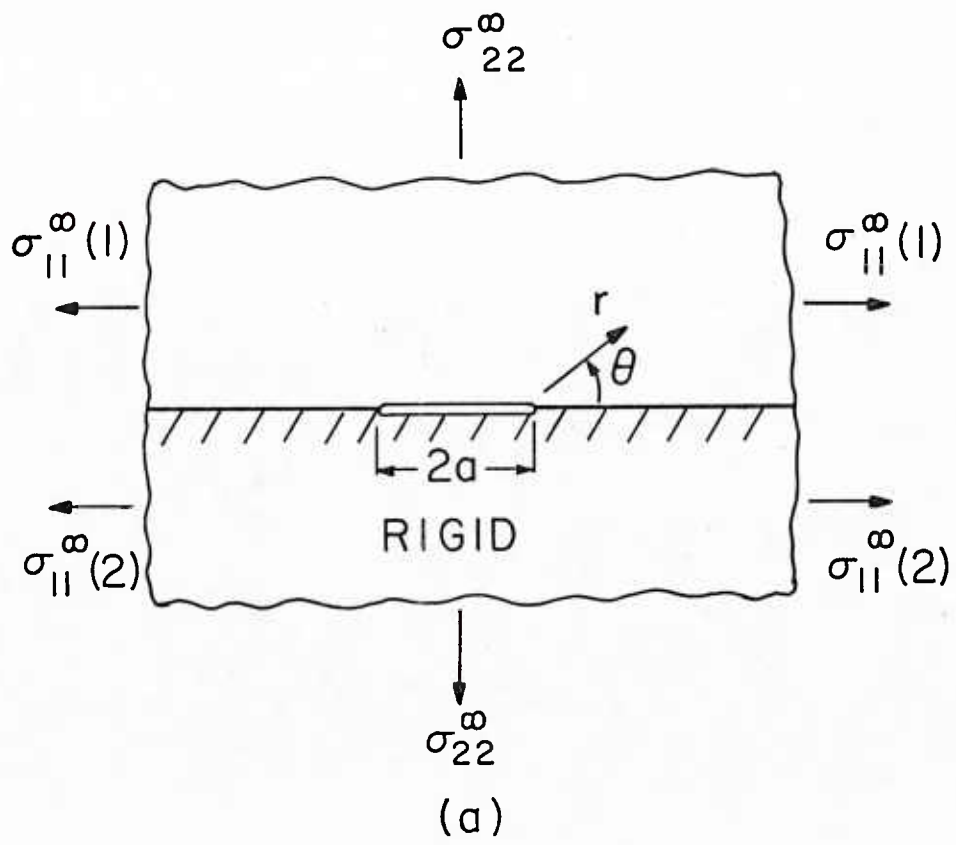


FIG. 3

(c)

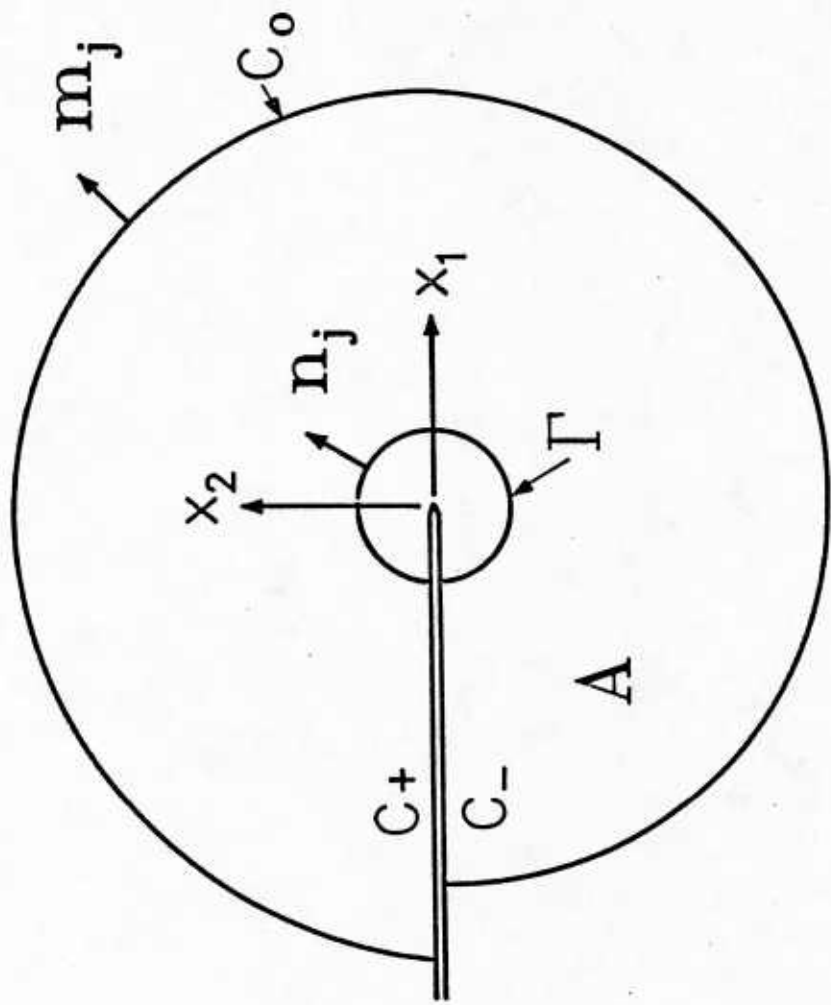


Fig. 4

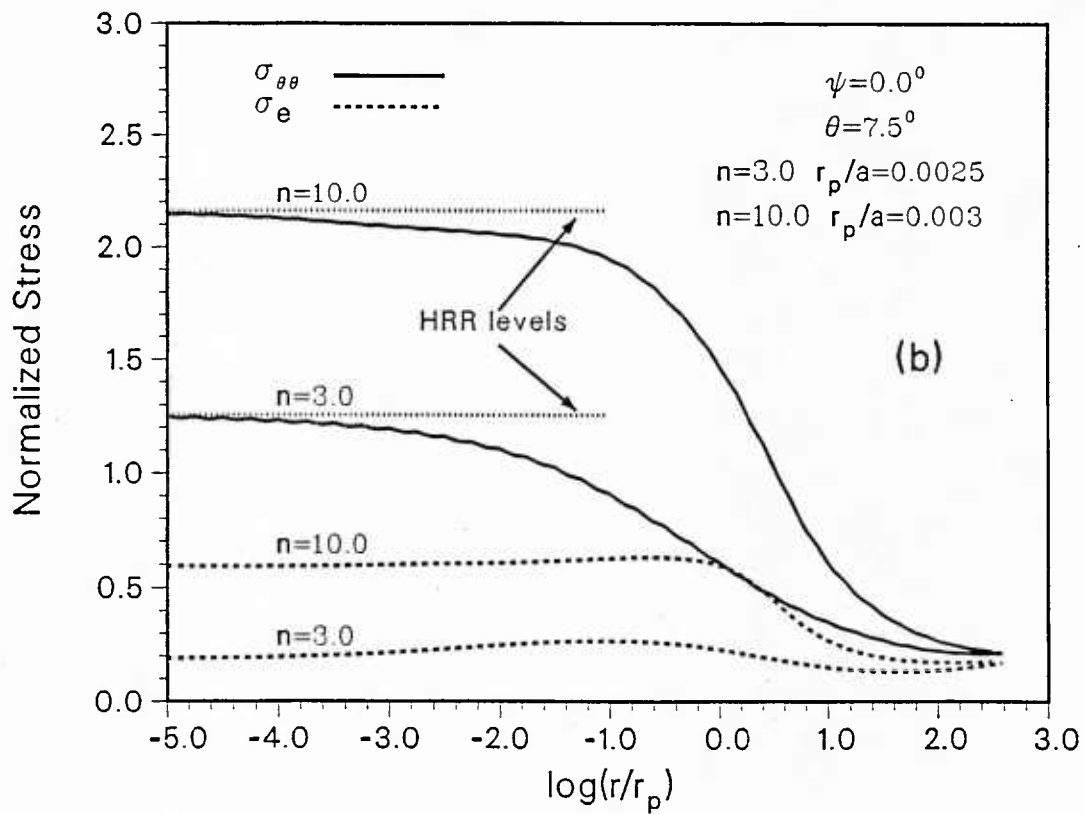
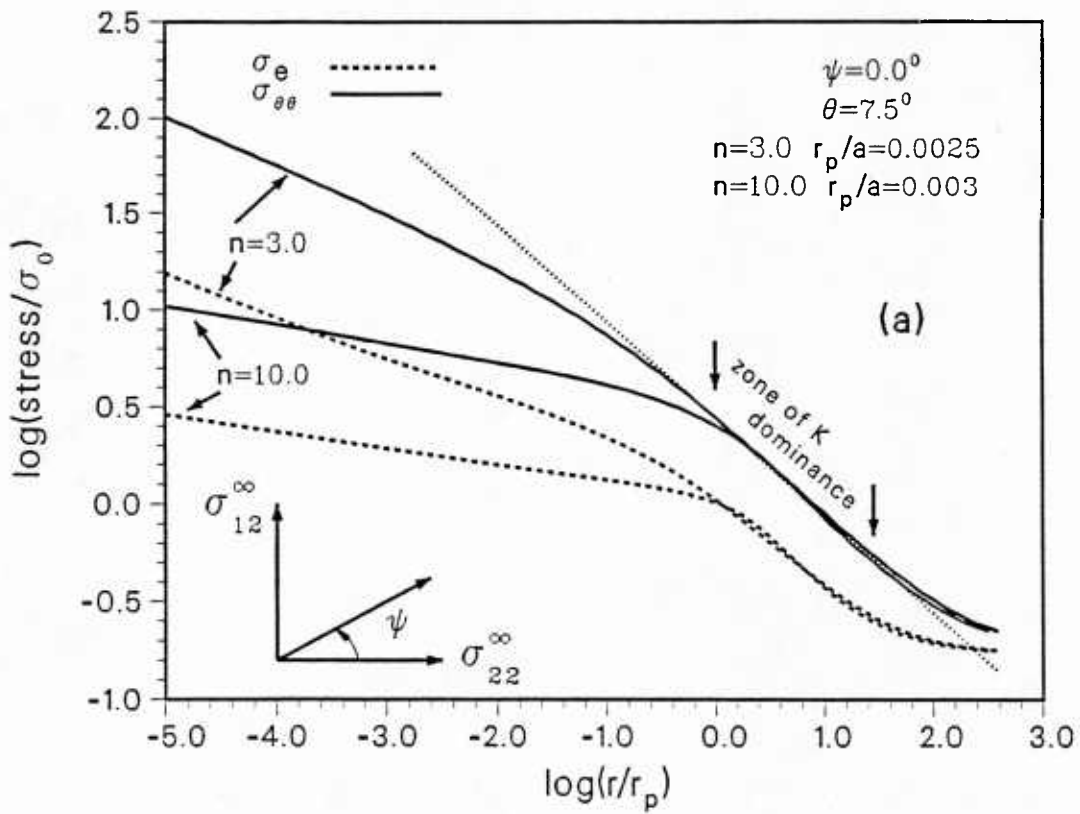


Fig. 5

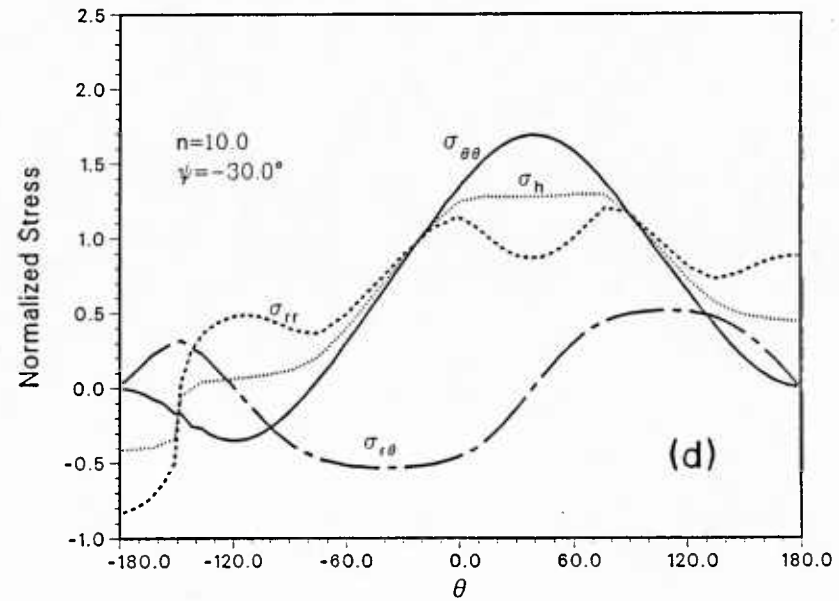
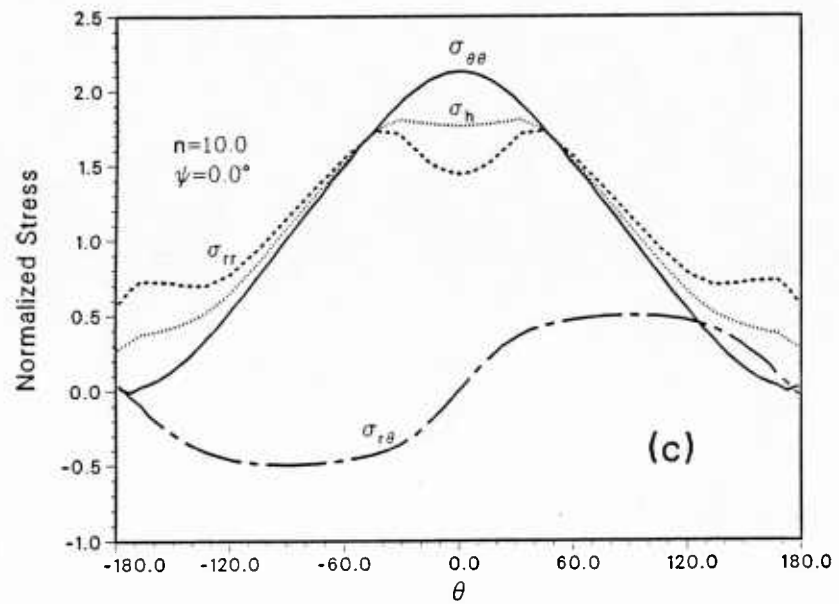
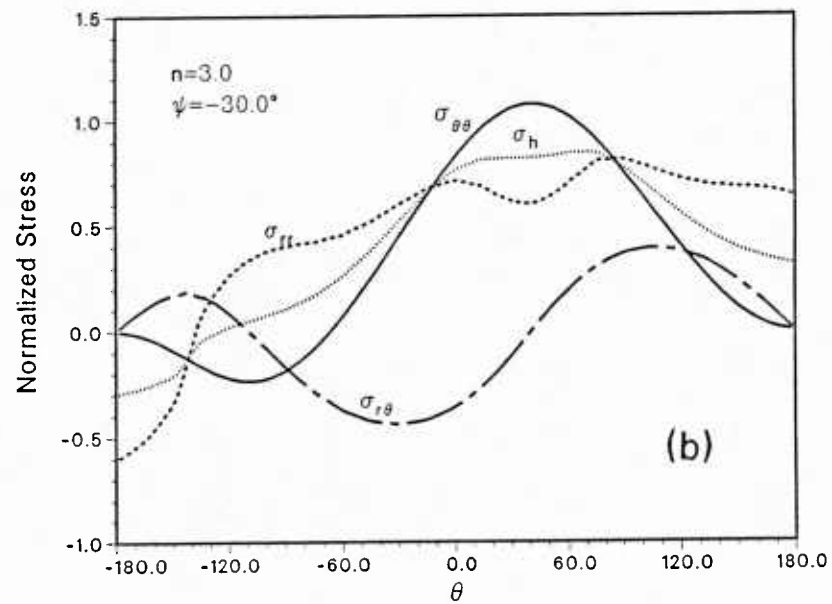
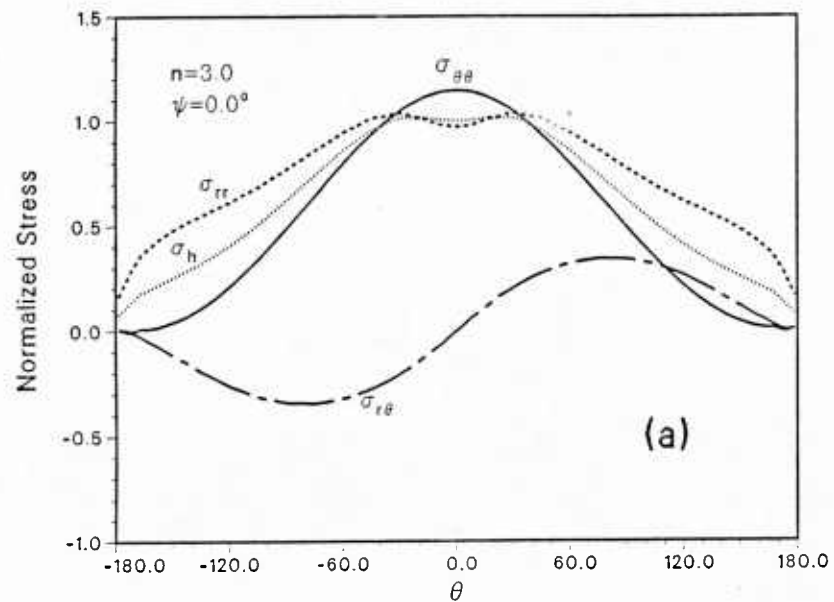


Fig. 6

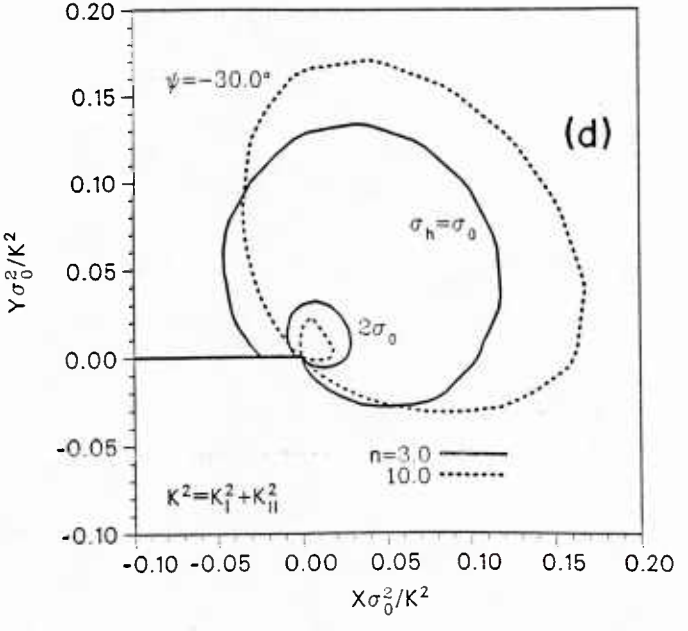
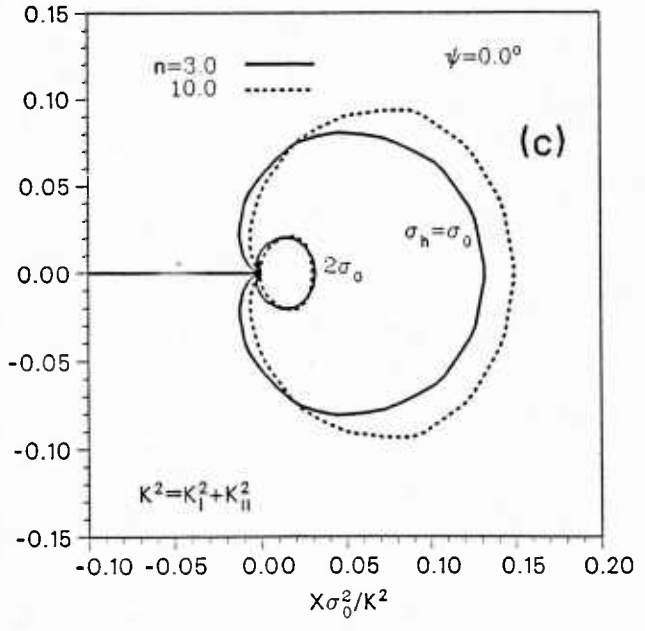
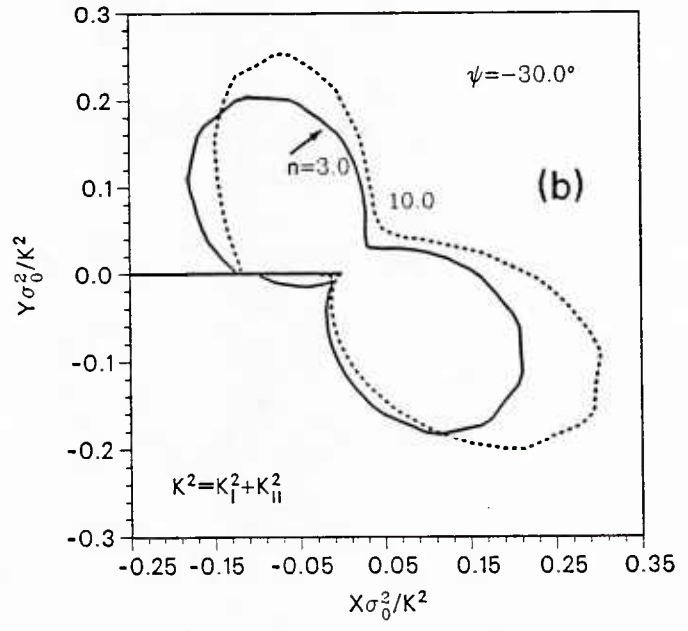
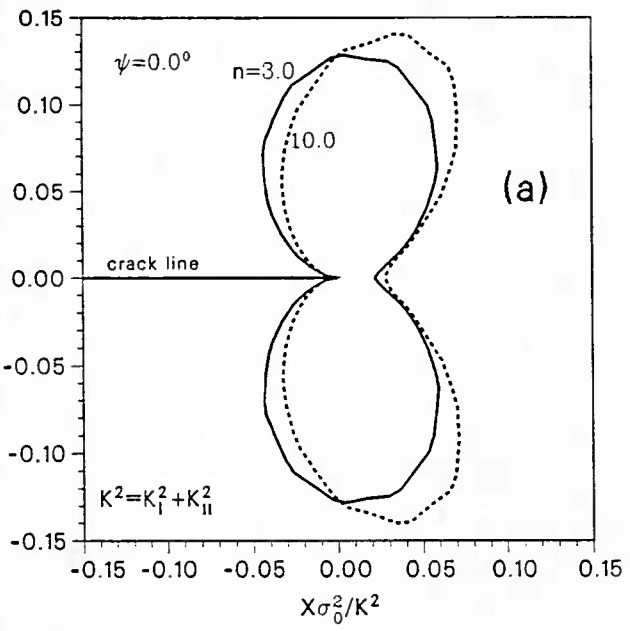


Fig. 7

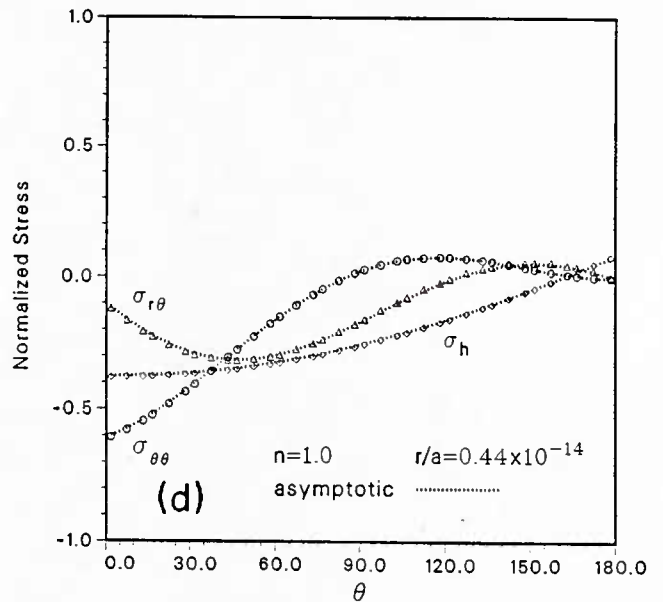
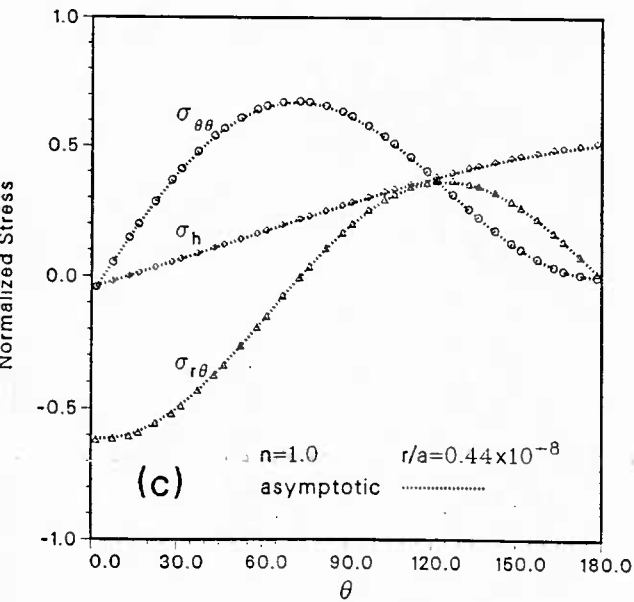
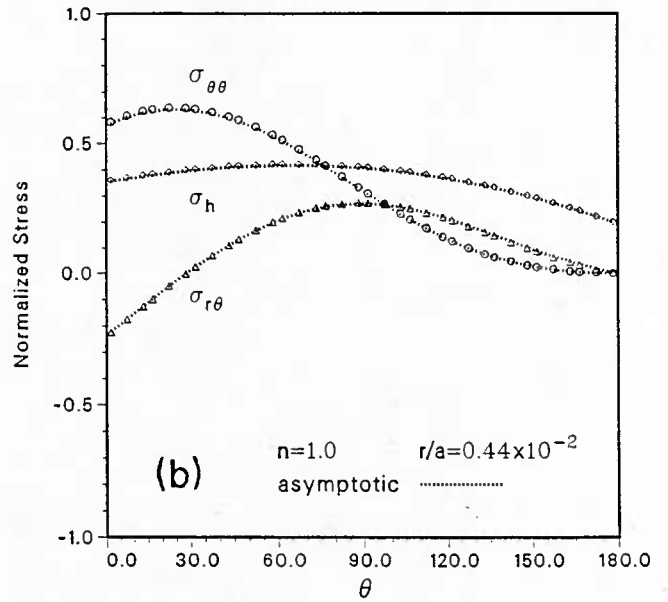
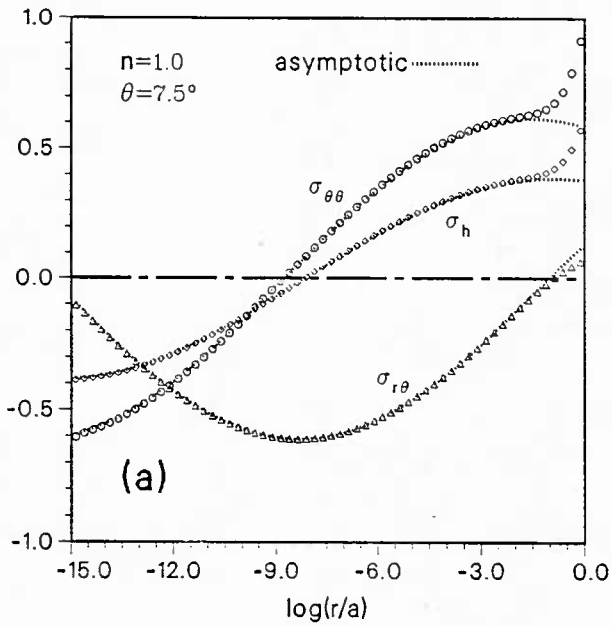


Fig. 8

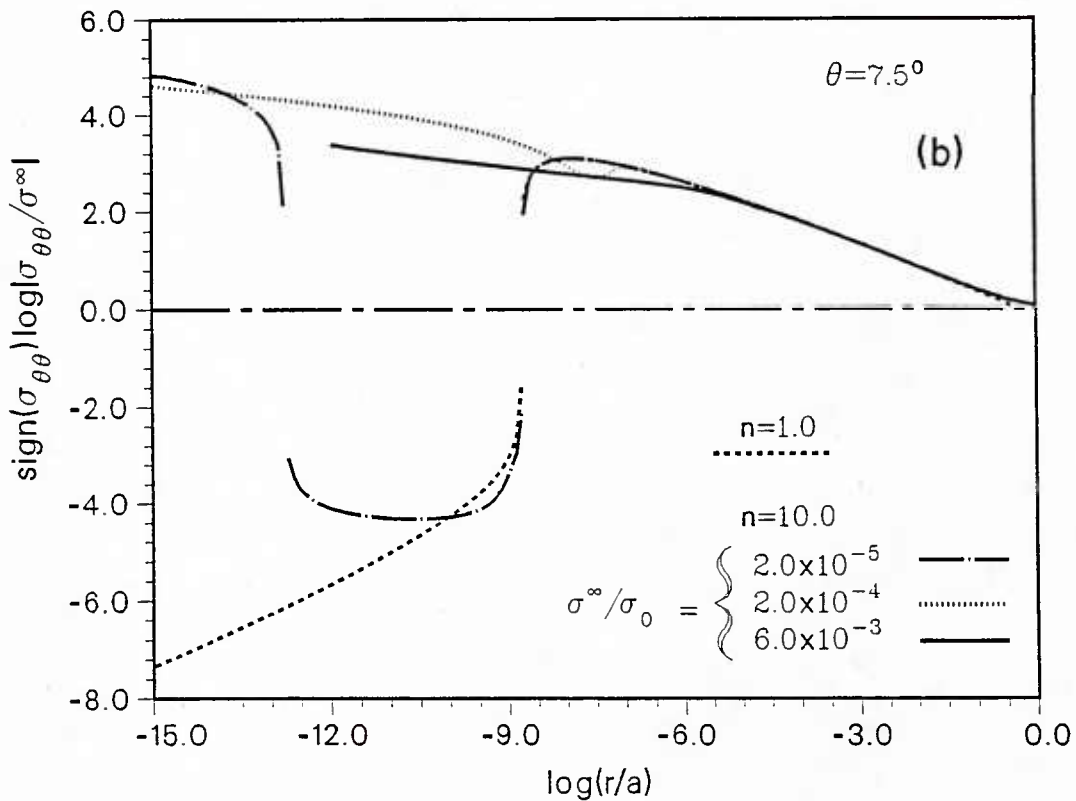
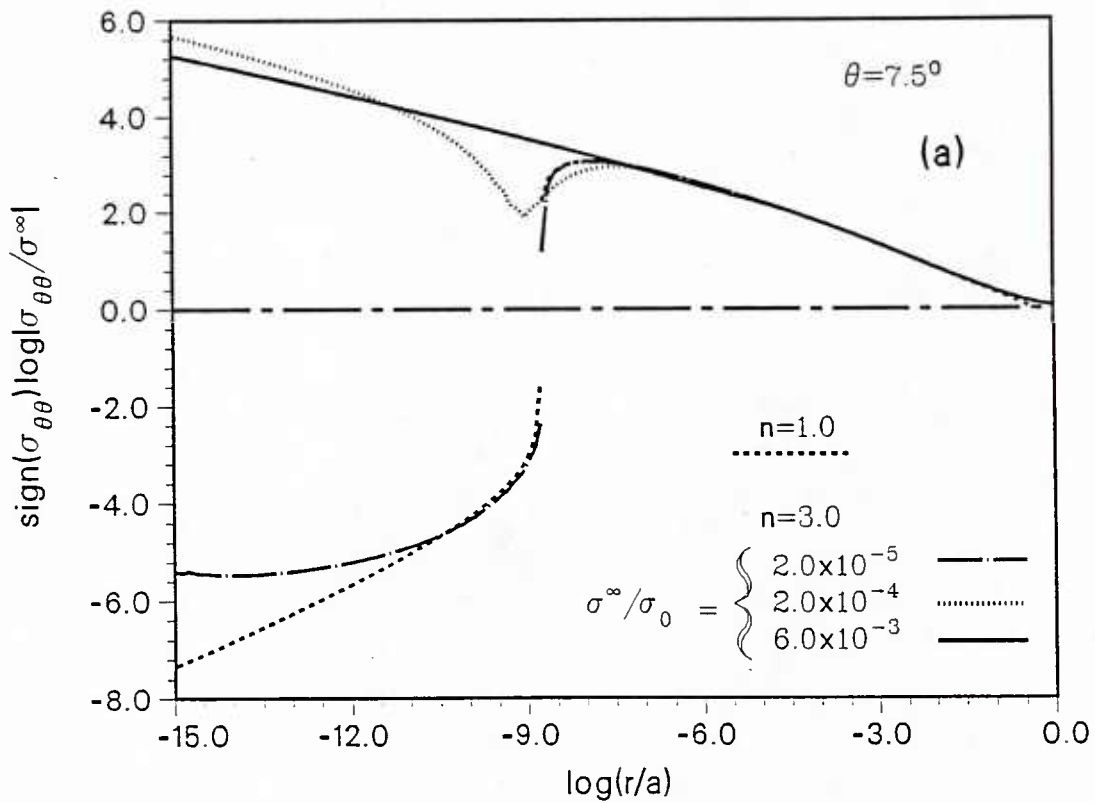


Fig. 9

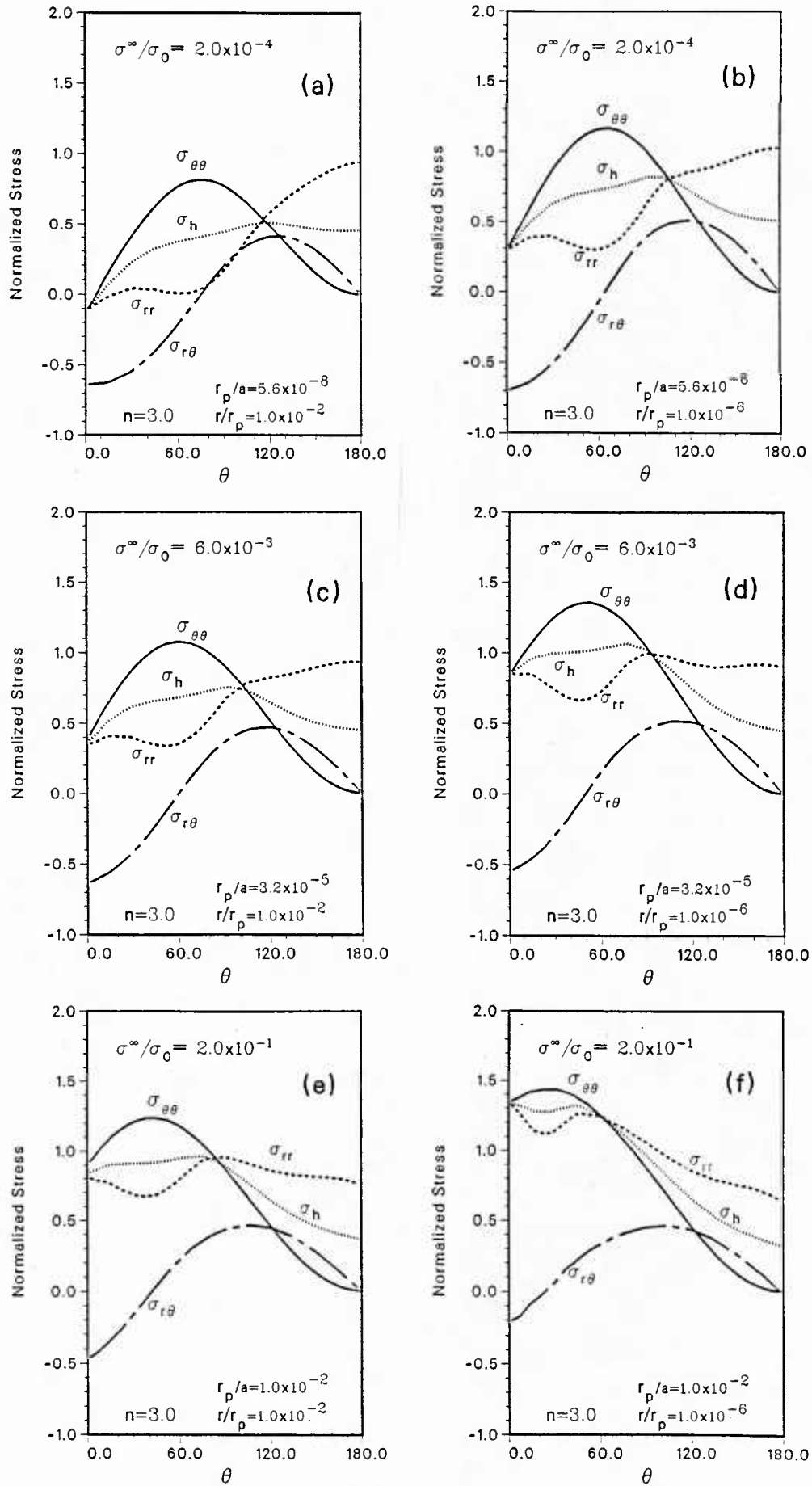


Fig. 10

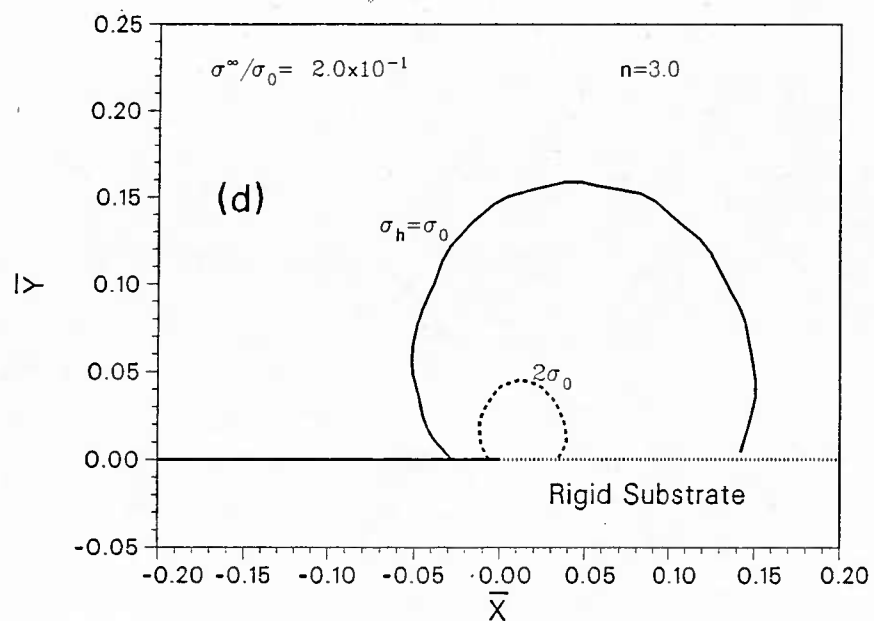
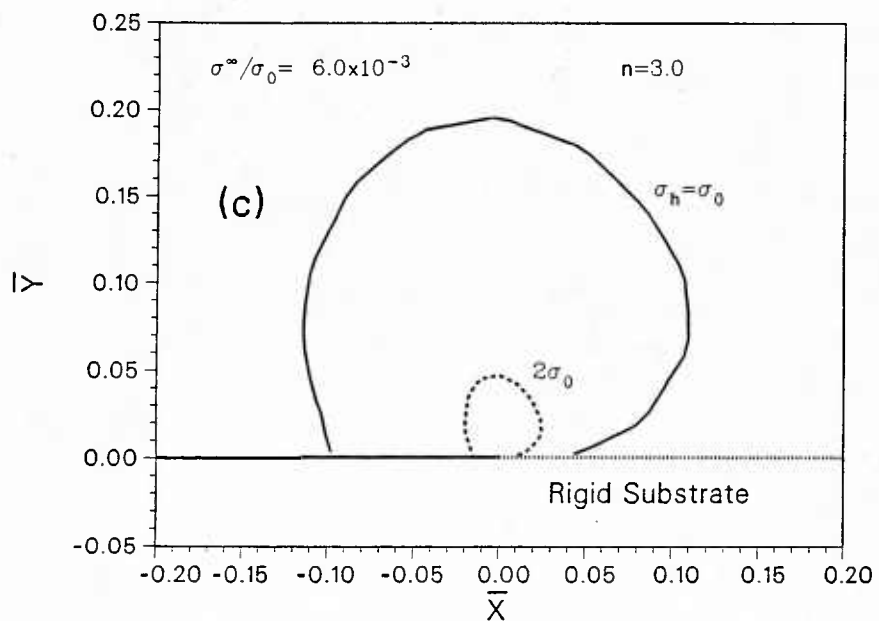
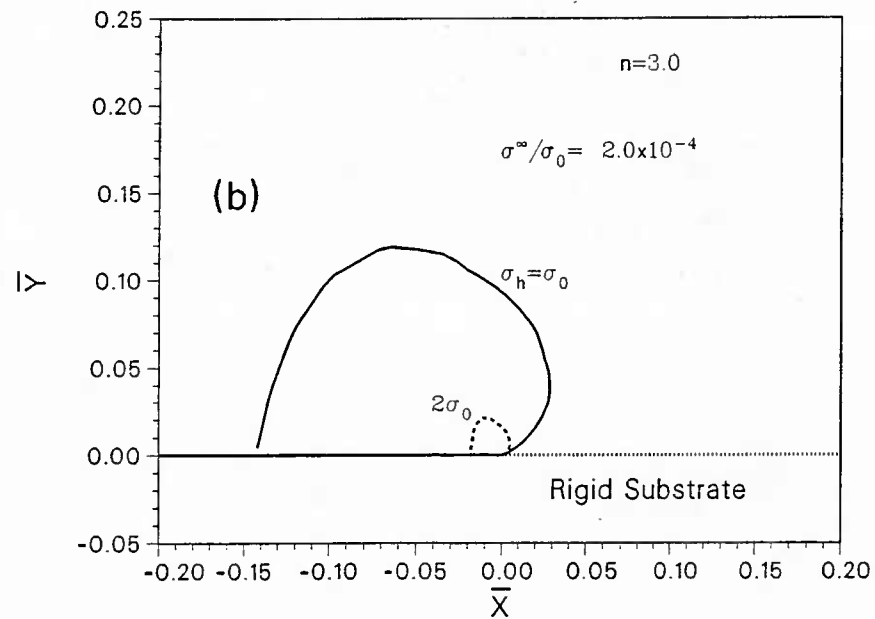
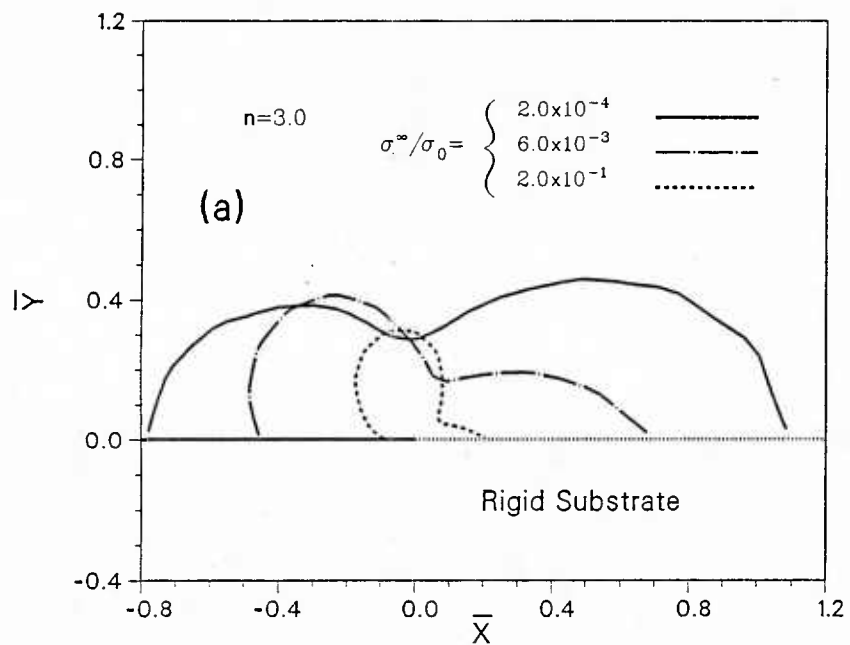


Fig. 11

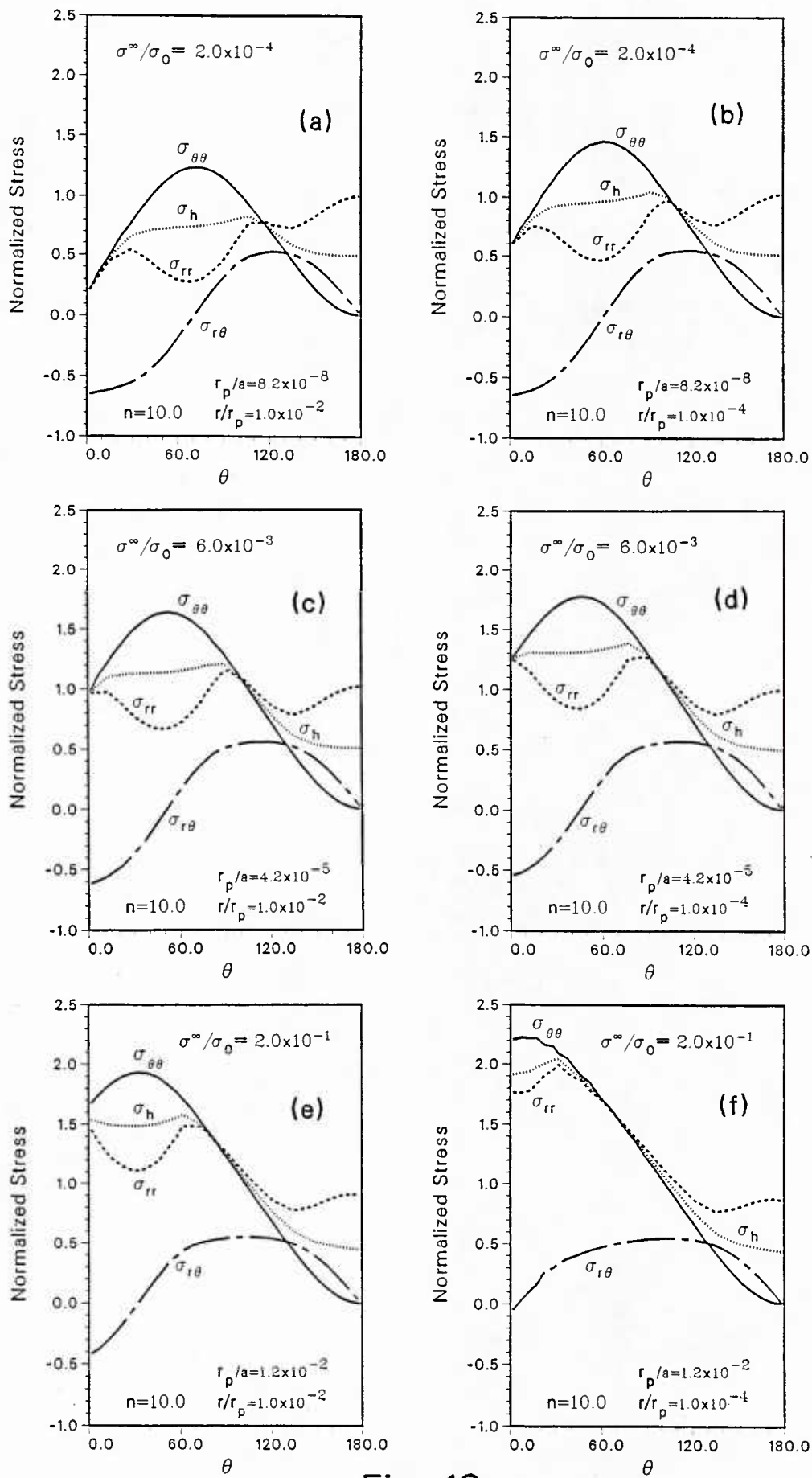


Fig. 12

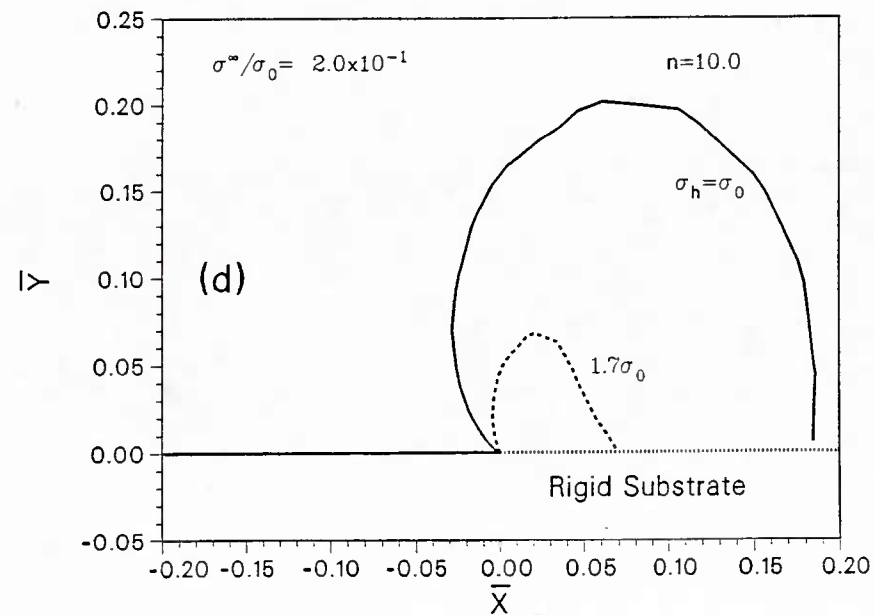
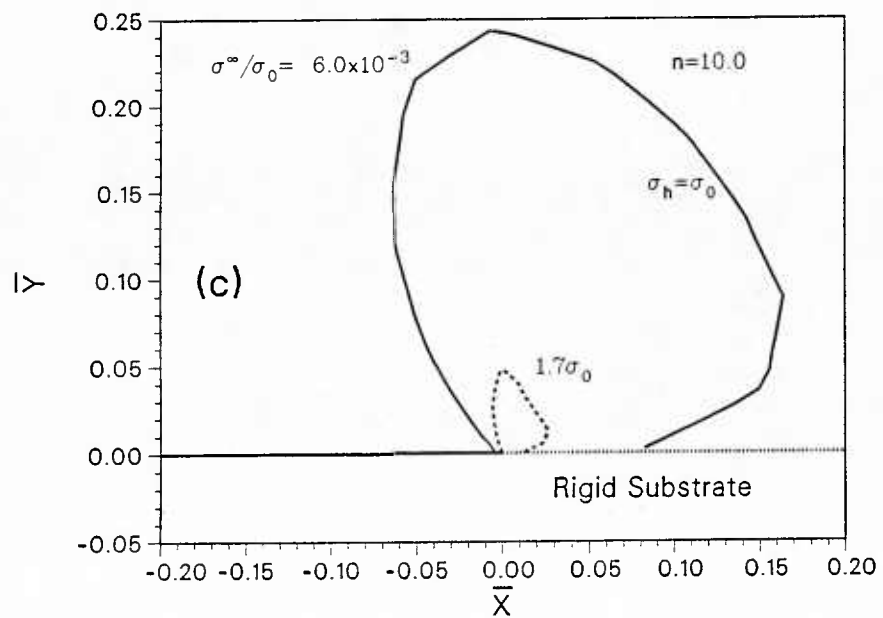
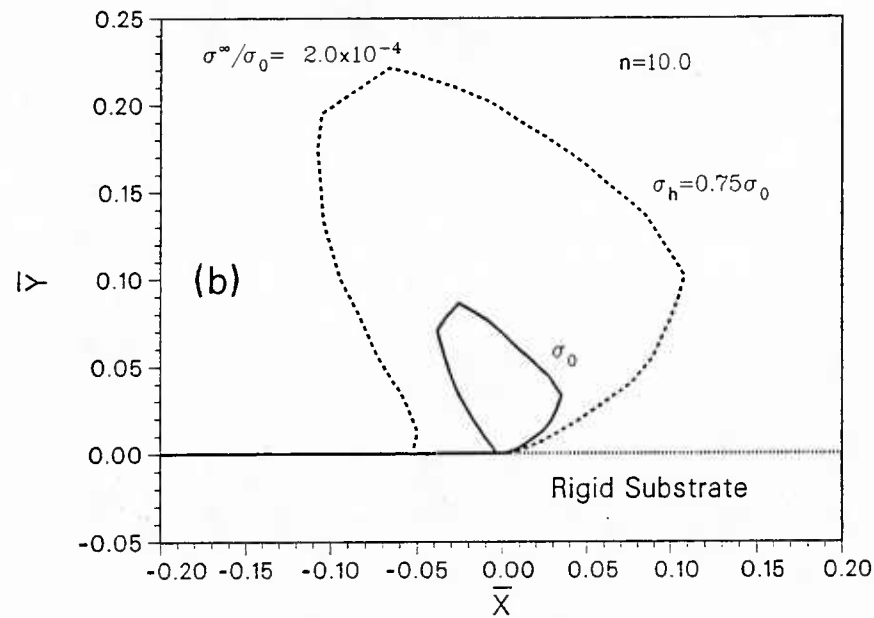
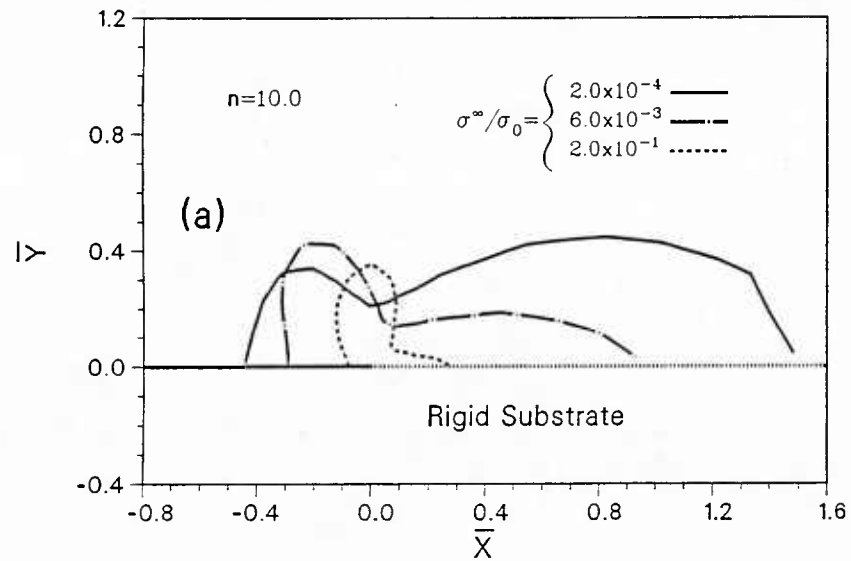


Fig. 13

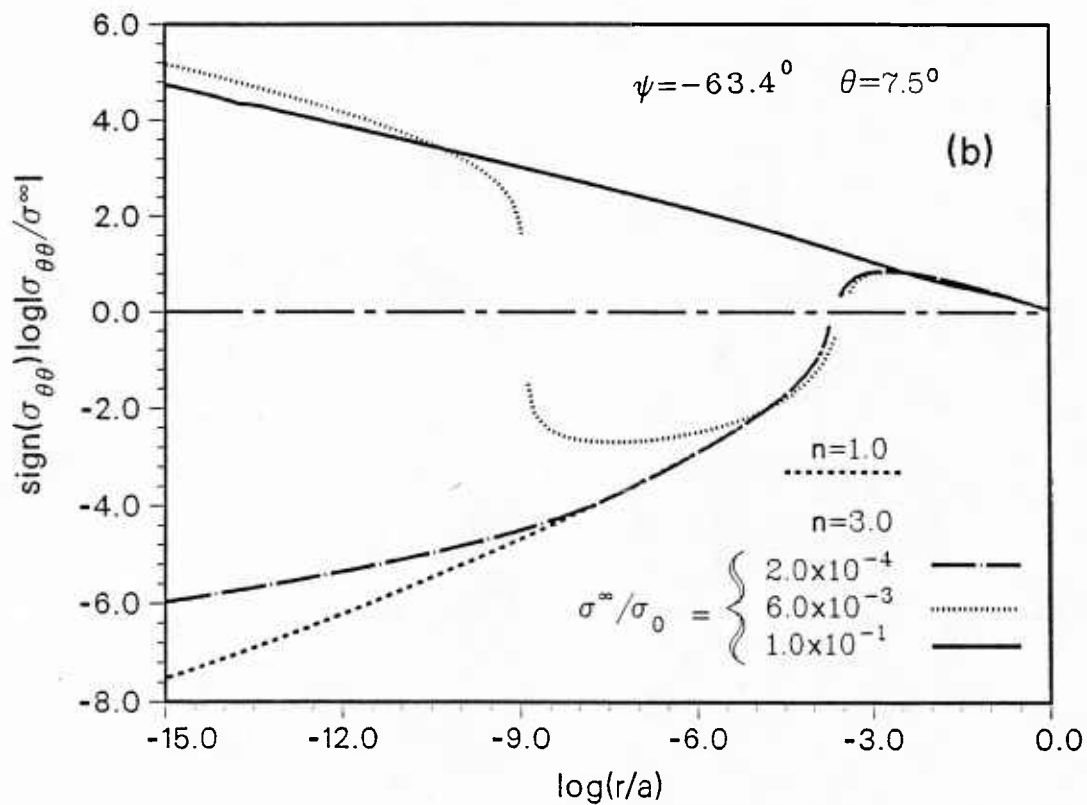
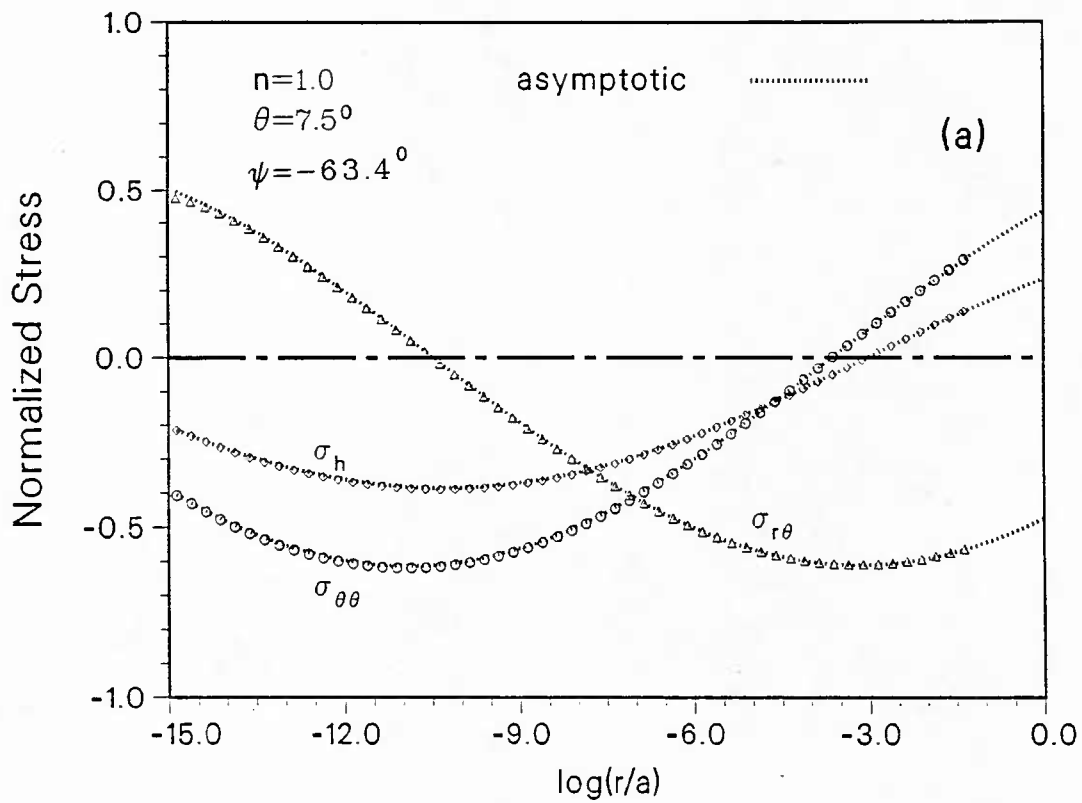


Fig. 14

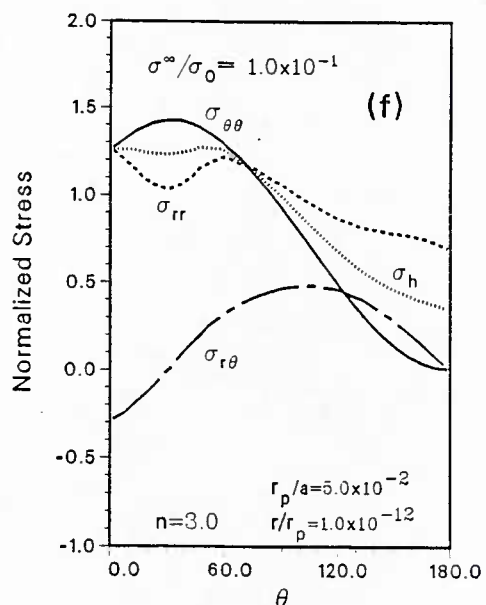
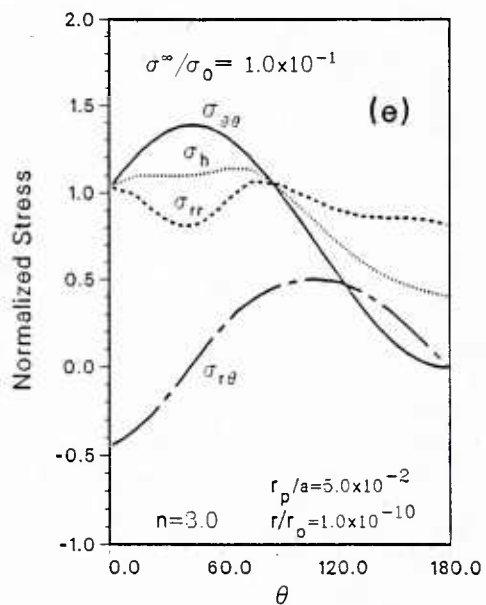
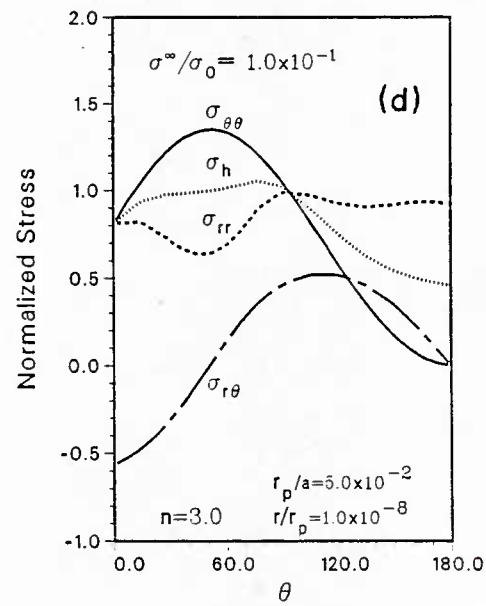
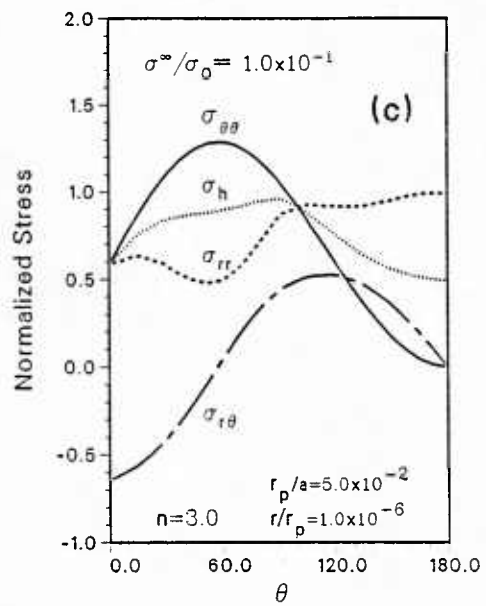
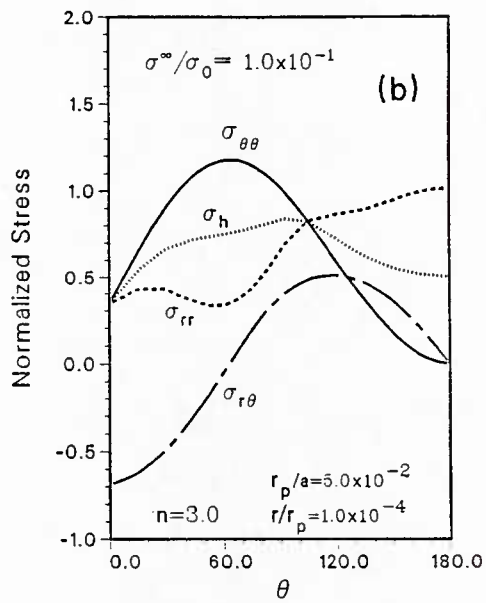
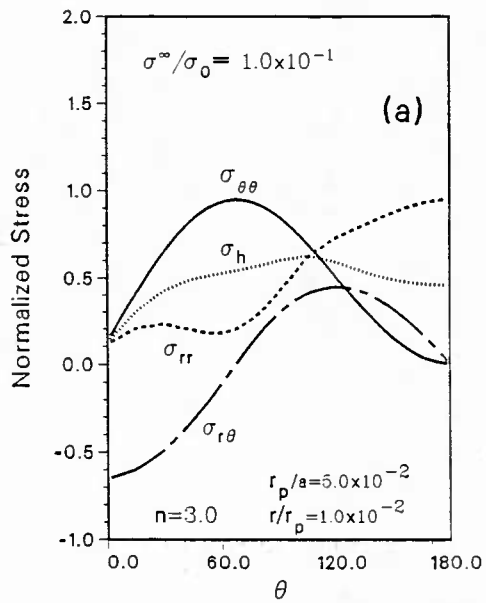


Fig. 15